



The composite radar-GNSS spectrum of auroral plasma turbulence

Magnus F Ivarsen^{1,2}, Kaili Song³, Luca Spogli⁴, Jean-Pierre St-Maurice^{1,5}, Devin R Huyghebaert^{6,1}, Brian Pitzel¹, Saif Marei¹, Yangyang Shen⁷, Satoshi Kasahara⁸, Kunihiro Keika⁸, Yoshizumi Miyoshi⁹, Tomo Hori⁹, Atsuki Shinbori⁹, Kazuhiro Yamamoto⁹, David R Themens¹⁰, P. T. Jayachandran³, Yoichi Kazama¹¹, Shiang-Yu Wang¹¹, Ayako Matsuoka¹², Iku Shinohara¹³, Takefumi Mitani¹³, Takeshi Takashima¹³, Shoichiro Yokota¹⁴, Yoshiya Kasahara¹⁵, and Glenn C Hussey¹

¹Department of Physics and Engineering Physics, University of Saskatchewan, Saskatoon, Canada

²The European Space Agency Centre for Earth Observation, Frascati, Italy

³Physics Department, University of New Brunswick, Fredericton, Canada

⁴Istituto Nazionale di Geofisica e Vulcanologia, Rome, Italy

⁵Department of Physics and Astronomy, University of Western Ontario, London, Canada

⁶Leibniz Institute of Atmospheric Physics, Kühlungsborn, Germany

⁷Department of Physics, University of Alberta, Edmonton, Canada

⁸Department of Earth and Planetary Science, University of Tokyo, Tokyo, Japan

⁹Institute for Space-Earth Environmental Research, Nagoya University, Nagoya, Japan

¹⁰School of Engineering, University of Birmingham, Birmingham, UK

¹¹Academia Sinica Institute of Astronomy and Astrophysics, Taipei, Taiwan

¹²Data Analysis Center for Geomagnetism and Space Magnetism, Kyoto University, Kyoto, Japan

¹³Institute of Space and Astronautical Science, Japan Aerospace Exploration Agency, Sagami-hara, Japan

¹⁴Department of Earth and Space Science, Osaka University, Toyonaka, Japan

¹⁵Graduate School of Natural Science and Technology, Kanazawa University, Kanazawa, Japan

Abstract. In the auroral ionosphere, plasma turbulence acts as an important dissipation mechanism for magnetospheric energy and the primary cause of radio wave scintillation. Characterizing auroral plasma turbulence across its full spatial extent has historically been limited by the narrow bandwidths of individual instruments. Our investigation approaches the problem of obtaining accurate, scale-dependent information using the physics of the Farley-Buneman (FB) instability, a modified two-stream plasma instability. In this study, we construct a composite spatial powerspectrum of plasma turbulence in the auroral electrojets spanning roughly four orders of magnitude in scale (from ~ 100 km down to ~ 20 m). This is achieved by combining a recent Monte-Carlo-based method of spatial clustering of very-high-frequency (VHF) radar echoes, with phase screen information derived from global navigation satellite system (GNSS) signals, using ground-based instrumentation in Canada. Through multi-instrument conjunctions with the European Swarm and Japanese Arase missions, we observe that the clustering of electrojet turbulence matches the structuring of field-aligned currents, and correlates with magnetospheric electron fluxes. Statistical analysis of the *composite* spectra, as well as a very large database of radar clustering spectra only, reveals a consistently steep decay of spectral power in the auroral electrojets, with the most probable spectral index being near $-8/3$. The observations suggest a continuous, scale-invariant cascade that frequently preserves the spatial signature of its magnetospheric drivers, where we outline a way for Alfvén waves to structure the turbulent E-region. Furthermore, we demonstrate that the plasma structures guilty of causing GPS scintillations (~ 270 meters in size) were moving at the ion acoustic speed, implying



that those structures were, in fact, FB waves, and we thereby establish an observational basis for low-frequency electrojet turbulence. The method that we present, the composite radar-GNSS spectra, will on both counts offer useful empirical constraints for future efforts seeking to simulate the “sub-grid” turbulence that complicates the magnetosphere-ionosphere coupling around aurorae.

20 1 Introduction

In Earth’s upper atmosphere, at the lower edge of the partially ionized layers of the ionosphere, intense plasma turbulence is observed during geomagnetic storms, in the form of crashing waves that appear inside the electrical currents of the auroral electrojets. Here, collisions between charged particles and neutral molecules become so frequent that the ratio of collision to cyclotron frequency is sufficiently large to demagnetize ions below 120 km, and demagnetize electrons below 80 km. The resulting difference in charge carrier mobility between 80 and 120 km allows strong electric fields in the aurora to drive Hall currents at times. For plasma drifts below around 400 m/s, the electrical currents remain laminar, but, when the electron drift speed exceeds the ion acoustic speed, C_s , the laminar current becomes unstable to electrostatic density fluctuations, triggering the Farley-Buneman (FB) instability through the ion inertia excited by the motion of the irregularities, which is driven by the electron plasma ($\mathbf{E} \times \mathbf{B}$) drift (Farley, 1963; Buneman, 1963).

30 Inside turbulent regions of the ionosphere, regions that can be several hundred kilometers in size, small-scale fluctuations in plasma density can disrupt traversing satellite navigation (GNSS) signals (Kintner P. M. et al., 2007; Jin et al., 2014), ultimately caused by the presence around aurorae of intense, broad-spectrum, electrostatic turbulence (Sato, 1972; Sudan and Keskinen, 1977; Fejer and Kelley, 1980; Keskinen, 1981; Huba et al., 1985). While plasma turbulence modulates radio signal phase and amplitude in ways that are detrimental to human technological progress (Moen et al., 2013), it also produces the ‘radio aurora’ (Hultqvist and Egeland, 1964; ?), the clear signature of aurorae, shown *solely* through the plasma turbulence that they create.

The problem of understanding this turbulence is therefore directly related to its effect on radio signals: what starts out as large-wavelength (ultra-low frequency, or ULF) waves generated by the solar wind at the bow shock or magnetopause of Earth (Krämer et al., 2024; Ivarsen et al., 2025c), will eventually produce the ~ 300 meter-size waves that disrupt GNSS signals (Song et al., 2023). This inherent and essentially non-linear coupling between the largest and smallest scales in geospace exacerbates the problem. The scale-dependent problem is tackled by turbulence physics, and its nature is typically inspected through application of Fourier analysis.

By elucidating the amount of fluctuation power in each individual wavenumber (or wavevector), Fourier analysis, in its many forms, can produce a *spectrum*, the power spectral density (PSD), and the shape of this spectrum is an expression of the scale-dependent physics that governs the overall turbulent cascade from the largest unstable magnetohydrodynamic (MHD) modes, to the small-scale kinetic plasma turbulence in Earth’s upper atmosphere, that we described at the onset of this Introduction.

45 In this paper, we present an observational model of the spectrum $P(k)$ of plasma turbulence in the auroral ionosphere, and this method spans almost four orders in magnitude in wavenumber k , with equivalent scale-sizes from 100 km down to around 20 m. We do this by combining two recent, novel methods of PSD estimation: a spatial spectrum based on Monte-



Carlo-simulations (Ivarsen et al., 2023a), and a temporal Fourier analysis of GNSS phase fluctuations (Song et al., 2025). The
50 former correlates the spatial positions of very-high frequency (VHF) coherent radar echoes from the turbulent electrojets on
scale-sizes between ~ 100 km and ~ 500 m, while the latter translates a temporal Fourier spectrum of GPS signals received
from the ground, to a spatial spectrum via phase screen theory, for scale-sizes between ~ 5 km to ~ 20 m.

We analyze the characteristics of the composite radar-GNSS spectrum around diffuse auroras and find that the composite
spectrum of plasma turbulence matches signatures in the field-aligned currents (FAC) inside the aurorae, consistent with recent
55 discoveries, and we find that spectral steepness correlates with observations of particle precipitation from the magnetosphere.
Surprisingly, we observe that the composite spectrum of plasma turbulence near aurorae seem *universally steep*, and *dissipative*,
with spectral indices that only approach inertial values on scale-sizes that are limited.

In what follows, in Section 2 we shall describe the two methods, and provide some details on spectral density interpre-
tation in ionospheric physics. We then present in Section 3 results from 10 case studies, including conjunction studies with
60 orbiting satellites, as well as statistical results from four years of radar data. In Section 4, we discuss the implications of our
results, where we argue that the detailed description of these spectra provide unique opportunities for fluid MHD models to
parameterize and verify the turbulent cascade that culminates in plasma turbulence smaller than those models can resolve.

2 Methodology

This section is a summary of recent papers of a highly technical nature, pertaining to coherent radar data from Ionospheric
65 Continuous-wave E-region Bistatic Experimental Auroral Radar (ICEBEAR) (Ivarsen et al., 2023a) and GPS signal analysis
from the Canadian High-Arctic Ionospheric Network (CHAIN) (Jayachandran et al., 2009; Song et al., 2025). At the end of this
section, we comment on current interpretations of spectral density measurements in the auroral ionosphere.

2.1 Pairwise VHF radar echo clustering

We analyze coherent scatter radar data from ICEBEAR, an experimental radar capable of imaging the distribution of small-scale
70 plasma turbulence in 3-dimensions (3D), (Huyghebaert et al., 2019; Lozinsky et al., 2022) yielding the ICEBEAR 3D dataset.
The radar's 6 m wavelength yields a 3 m Bragg wavelength, meaning we observe meter-scale turbulent waves. The turbulence
echoes are seen towards the northern horizon in Saskatchewan, Canada.

ICEBEAR can record thousands of echo locations per second, yielding exceedingly large point-cloud datasets, (Ivarsen et al.,
2023c, 2024c) and we are in this paper segmenting the radar data in 6 second bins. The radar echoes observed inside each bin
75 are clustered using `dbscan` following Ivarsen et al. (2024c).

Ivarsen et al. (2023a) developed a method to correlate the pairwise spatial positions of each imaginable pair of echoes found
inside such radar echo point-clouds, using the *two-point correlation function*, $\xi(r)$,

$$n^2[1 + \xi(r)] = \langle \rho(x)\rho(x+r) \rangle, \quad (1)$$



where n is the average number density of echoes in a given volume, and $\rho(x)$ is the number density of echoes at location x ,
80 and r is a distance away from x , and in Figure 2c) we show $\xi(r)$ calculated for the cluster shown in Figure 2b). The method
yields spatial power spectra $P(k)$ through a Hankel transform, (Ivarsen et al., 2016; Baddour, 2011)

$$P(k) = \int_0^{\infty} \xi(r) J_0(kr) r dr, \quad (2)$$

where $J_0(kr)$ are zeroth order Bessel functions of the first kind. Such power spectra yield spectral information roughly between
the scale-sizes 750 m and $\sim 10^5$ m, much larger than the ICEBEAR radar wavelength (3 m). Later, the spectra were demonstrated
85 to match the small-scale structuring of field-aligned electrical currents associated with pulsating aurorae (Ivarsen et al., 2024a)
as well as F-region plasma structuring. (Ivarsen et al., 2023b)

2.2 E-region target radar motions

To complement pairwise echo clustering, we exploit the recent discovery that a 3D coherent radar such as ICEBEAR can
be operated as a target radar, by identifying and tracking coherent clusters of radar echoes through time and space (Ivarsen
90 et al., 2024c). The method, which was tested against actual displays, relies on an unsupervised machine learning algorithm to
automatically identify dense clusters of radar echoes, before it quantifies the spatial trajectories of such clusters. This yields
the actual $\mathbf{E} \times \mathbf{B}$ motion of the source regions, which have to be the same as the F-region plasma velocities normally observed
just in the F region (Ivarsen et al., 2024c, d, 2025c). This method overcomes the well-known fact that coherent E-region radars
normally observe structures moving close to, or below, the ion acoustic speed of the turbulent auroral E-region owing to the
95 nonlinear properties of large amplitude Farley-Buneman waves observed by coherent E-region radars (e.g., Fejer and Kelley,
1980; Sahr and Fejer, 1996). It has been clearly shown that the difference between the two velocities can be considerable under
strong electric field conditions [e.g., Figure 2 in Foster and Erickson (2000), and references therein].

In Figure 1 we present a typical example, tracked ICEBEAR echo cluster, superposed on auroral imaging by TREX (RGB,
2023). The cluster's *centre-of-mass*, or median echo location, moved around 24 kilometers in the magnetic north-east direction,
100 tracked for a 25-second duration. That yields a target motion of some 1300 m/s, and these target motions, really the transatory
displacement of echo centres-of-mass, have been demonstrated to track the wider ionospheric “frozen-in” drift (Ivarsen et al.,
2024c, d, 2025c). In Figure 1, the 1300 m/s tracked motion, much faster than the ~ 350 m/s speed obtained from the radar
echo Doppler shifts, corresponds to a 74 mV/m electric field. We note that a unique feature in the analysis of echo cluster 898
(Figure 1) is the fact that we have tracked this cluster as *descended* slightly, moving downward with a speed of 330 m/s; the
105 first instance of quantifying the vertical descent of a coherent plasma structure in the auroral E-region.

2.3 GPS phase fluctuations and the phase-screen drifts

To complement tracking and radar spectral analysis of echo locations, we perform a time-series analysis of GPS amplitude and
phase fluctuations measured with the Ionospheric Scintillation Monitor Receiver (ISMR) located at the Rabbit Lake research
station (58.23°N, 256.32°E), which is part of the Canadian High Arctic Ionospheric Network (CHAIN Jayachandran et al.,

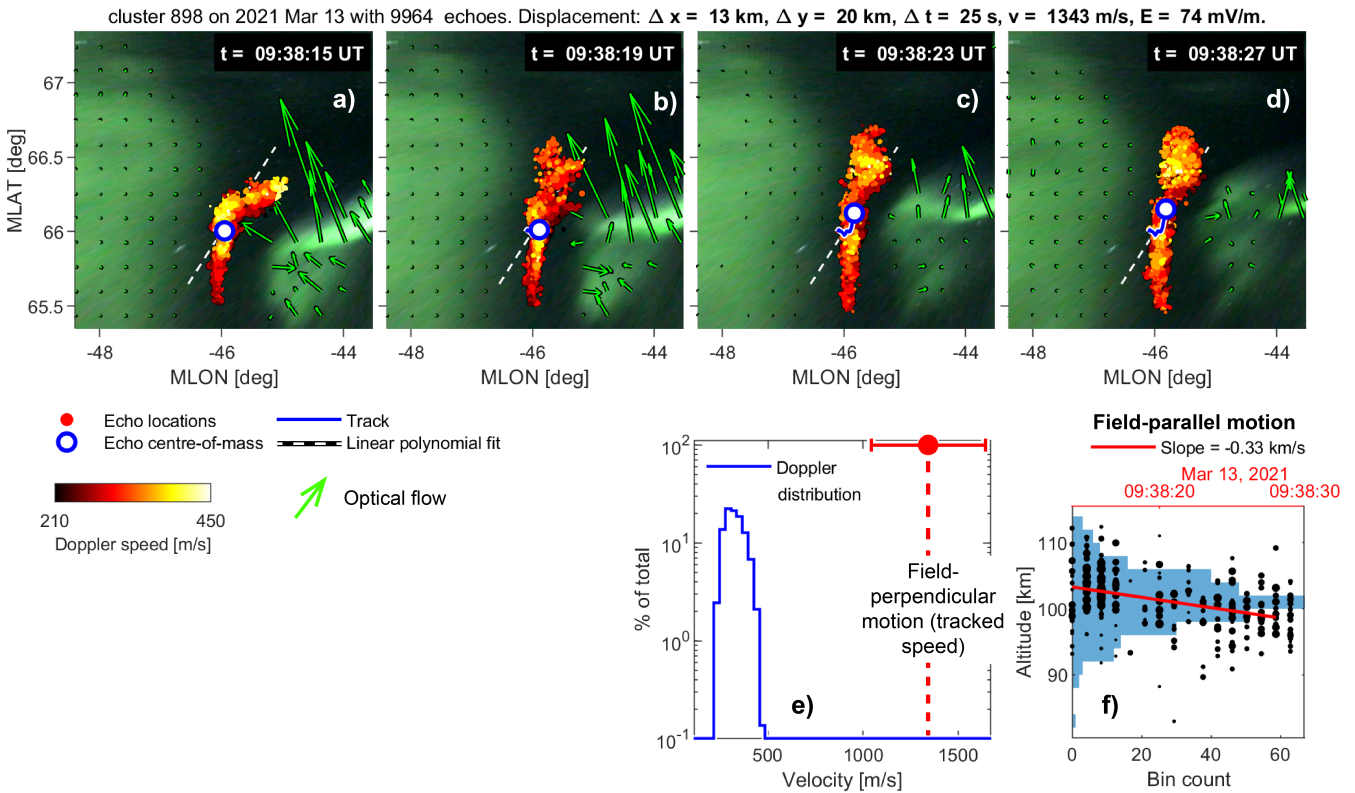


Figure 1. Panels a–d): Identifying & tracking a cluster of VHF radar echoes, emanating from Farley-Buneman turbulence between two auroral forms. Echo point-clouds are color-coded by Doppler speed, and superposed on optical aurora images using the TREX RGB (Gillies et al., 2020) camera located at Rabbit Lake, with green arrows showing the Horn-Schunk method of optical flow vectors Barron et al. (1994), applied to the green channel of the auroral images [see Ivarsen et al. (2024d) for details of such conjunction studies]. **Panel e)** contrasts the Doppler speeds with the tracked, target motion, while **Panel f)** shows the altitude distribution of this cluster, with the echo altitude cloud in a scatterplot (top, red axis).

110 2009). The ISMR in Rabbit Lake is a Septentrio PolaRxS, (Bougard et al., 2011) capable of recording the raw phase and post-correlation in-phase (I) and quadrature (Q) samples of GNSS signals at a 100 Hz sampling rate. For the purposes of our work, we concentrate solely on GPS.

The signals emitted by GPS satellites and subsequently recorded by the ISMR are disrupted by plasma irregularities linked with instabilities and resultant turbulent phenomena in the ionospheric plasma, (Yeh and Liu, 1982; Kintner P. M. et al., 115 2007). This introduces stochastic fluctuations in the recorded signal amplitude (McCaffrey and Jayachandran, 2019; Spogli et al., 2021; Ghobadi et al., 2020; Song et al., 2023; Meziane et al., 2023) .We derive a spatial k -spectrum from the temporal fluctuations in the recorded signal in the Rabbit Lake ISMR (directly beneath the radar field-of-view) using phase screen theory (Yeh and Liu, 1982) . In this framework, the Fresnel frequency f_F is derived from the second zero-crossing of the normalized cross-spectrum of the L1-L2 or L1-L5 carrier frequencies, (Song et al., 2025) or, equivalently, the prominent breakpoint or



120 “knee” in the ionosphere-free linear combination (IFLC) spectrum, (Song et al., 2025), shown with a blue line in Figure 2d). We then estimate the average drift velocity \mathbf{v}_d of the irregular structures in the region where they originate (Forte and Radicella, 2002; Spogli et al., 2021), using $v_d = f_F \lambda_F$, where λ_F is the corrected Fresnel scale (Ghidoni et al., 2025),

$$\lambda_F = \frac{\sqrt{2\lambda_{\text{GPS}}h}}{\sin^{3/2}\theta}, \quad (3)$$

where $\lambda_{\text{GPS}} \approx 20$ cm is the wavelength of the GPS signal, θ is the GPS satellite elevation angle, and h is the altitude of
125 the irregularity layer, here assumed to be around $h = 105$ km (see Appendix C for a sensitivity analysis of this assumption). The expression for λ_F takes into account the oblique incidence observational geometry, for which the distance between the antenna and the irregularity layer becomes $h \sin \theta$. We estimate the irregularity velocity under the approximation of a single, thin layer. While we account for the azimuthal dependence introduced by the elliptical projection of the scan path under anisotropic conditions (Teunissen and Montenbruck, 2017), we do not apply an axial ratio correction to the Fresnel scale λ_F
130 itself, effectively treating the base irregularities as isotropic. The velocity measured with this method yields an estimate of the relative velocity between the satellite pierce-point and the ionospheric irregularities, often referred to as “scan velocity”. (Yeh and Liu, 1982)

We construct a spectrum based on the IFLC spectrum (for scale-sizes smaller than the Fresnel scale), and a spectrum of Total Electron Content (TEC) fluctuations for scale-sizes larger than that threshold. The result is a k -spectrum that yields spectral
135 information on scales roughly between 5 km and ~ 20 m (the red spectrum in Figure 2d), which is readily compared to the spectrum of “echo clustering” of co-located irregular structures seen by radar.

The two spectra, one from radar and one from GNSS, are then simply spliced (see Figure A1 in the Appendix A): the two spectra feature an overlapping transition zone spanning spatial scales roughly between 750 m and 3000 m. To avoid artifacts from spectral leakage, we truncate the radar spectrum for scales smaller than 750 m, and the GNSS spectrum for scales larger
140 than 3000 m. Within this overlapping regime, the spectral shapes from the two independent methods match strikingly well.

In addition to spectral inferences, the GPS-derived scan velocity could readily be compared to both the radar Doppler and target velocities. As discussed above, the target velocities reveal the true $\mathbf{E} \times \mathbf{B}$ -drift, while the Doppler shifts normally should not exceed an ion-acoustic speed of about 400 to 450 m/s if they come from near 100 km altitude. As it turned out, for a strong electric field event that we studied in detail, the observed GPS scan velocities were highly consistent with the upper limit of
145 the Doppler shift E region radar observations found at the ion-acoustic speed near 100 km altitude (see Figures 4 and 9 below). Those speeds were, in turn, far smaller than the bulk of the target speeds in the region. The most plausible interpretation of this unexpected result is that the 270 m structures associated with the Fresnel zone near 105 km were themselves nonlinear Farley-Buneman waves. This is the only explanation we could think of for their motion at the ion-acoustic speed. Indeed, there is no law to state that Farley-Buneman waves cannot exist at 270 m, although the growth rate from ion inertial has to exceed
150 that from the gradient-drift instability. This would only be expected for very strong electric fields (or for geometries in which the ambient density gradients are perpendicular to the ambient electric field, which is not very likely).

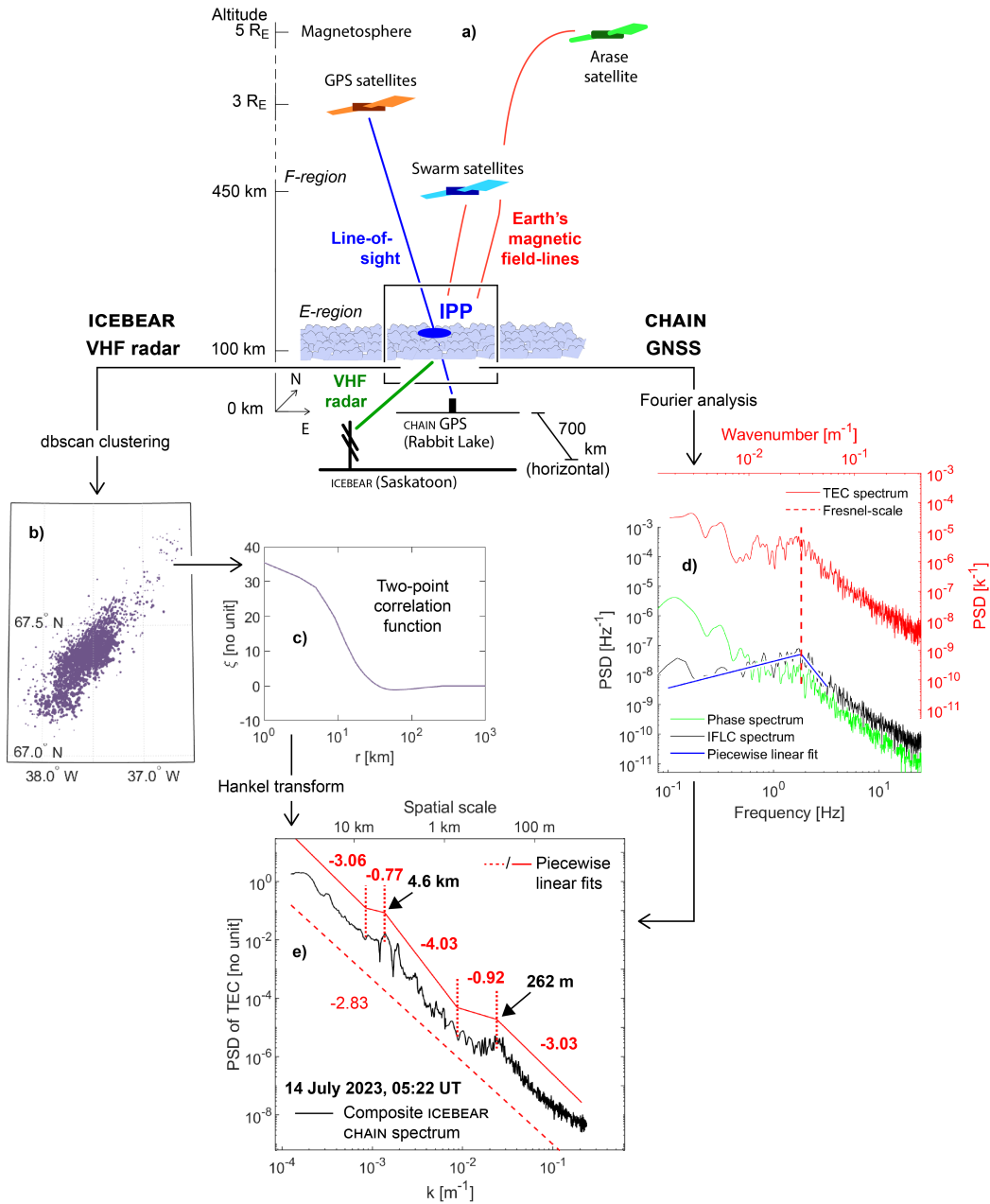


Figure 2. Panel a) shows a schematic overview of the observational space, with the various instruments, and the measurement geometry, annotated. Panel b) shows a sample 6-second radar point-cloud cluster, while Panel c) shows the two-point correlation function based on that point-cloud (Eq. 1). Panel d) shows example phase (green), IFLC (black), and TEC (red) spectra, with a piecewise linear fit shown with a blue line, and with the Fresnel scale (wavenumber) shown with a red, dashed line, based on measurements performed in the two-minute interval starting at 05:21 UT on 14 July 2023. Panel e) shows the resulting composite radar-GNSS spectrum for that interval, where the two-point correlation function of all nearby echo clusters have been Hankel-transformed to yield an average clustering spectrum. A five-component piecewise linear fit (solid red line) and a single linear fit (dashed red line) are shown above and below the spectrum respectively, with spectral indices posted in red.



2.4 Spectral density interpretation

The result from combining the two methods of spectral density measurements described in the foregoing section is presented in Figure 2e), in the form of the *composite radar-GNSS spectrum*, the primary observable analyzed in the present study. The clustering spectrum is seamlessly consistent with the TEC spectrum. Prominent breakpoints are seen at spatial scales 4.6 km and 262 m, and the inferred spectral index (see Eq. 4) is similar for the largest (> 50 km) and smallest (< 100 m) scale-sizes. What follows is a reflection on the role of such spectral density measurements in ionospheric plasma.

In studies of space plasma turbulence, one expects spectral densities to adhere to a simple power law if not for the full wavenumber range, at least for substantial wavenumber intervals (Phelps and Sagalyn, 1976; Tsunoda, 1988; Spicher et al., 2014), meaning that the spectra are categorized with equations of the type

$$P(k) \propto k^{-\alpha}, \quad (4)$$

where $P(k)$ is the power spectral density, k denotes wavenumber ($k = 2\pi/L$, L being spatial scale), and α is a positive constant describing the decay in spectral power with decreasing spatial scale (increasing k) (Sudan et al., 1973; Mounir et al., 1991; Ivarsen et al., 2021). α is referred to as the spectral index and is a central quantity of measurement in the present study. As just stated above, in the auroral region of Earth's ionosphere, the steady decay in power indicated by Eq. (4) needs to often be broken into segments, with typical 'break-points' occurring on spatial scales between 1 km – 5 km (Villain et al., 1986; Ivarsen et al., 2024e, 2023b) and between 30 m – 300 m (Basu et al., 1990; Mounir et al., 1991; Spicher et al., 2014; Hamza et al., 2023), in clear agreement with Figure 2e).

Break-points are often thought of as transition markers between inertial and fully collisional regimes in the F region (Keskinen and Huba, 1990; Kivanc and Heelis, 1998), or they can be viewed as "injection wavelengths" if the break points go through a peak. The injection wavelengths or the knees and the various spectral indices, or slopes, and relative magnitudes, are all, in the end, indicative of various scale-dependent instability processes that contribute to the structuring of the plasma (Sudan et al., 1973; Mounir et al., 1991).

Another view posits that measured spectral density is produced by the dimensionality constraints that are placed on the system, in which the emergence of ordered dissipative structures are as much a *consequence* and a *source* of chaos, (Marov and Kolesnichenko, 2013) and where spectral shape is dictated by *self-organized criticality*, (Marek and Schreiber, 2022) from which all the structure of the universe can presumptively be deduced.

3 Results

We shall start by presenting two ground-ground conjunctions between the VHF radar ICEBEAR and a CHAIN GPS receiver at Rabbit Lake. The first event (Figure 3) revolves around a relatively brief, two-minute conjunction, and the second event (Figure 4) details an extended one-hour conjunction.

The first, Figure 3a), exhibits a number of radar echo clusters being tracked, seen moving past a GPS ionospheric pierce-point (IPP), with a north-eastern bearing. Figure 3c, d) detail the strong temporal correlation ($\rho = 0.94$) between the rate of detected

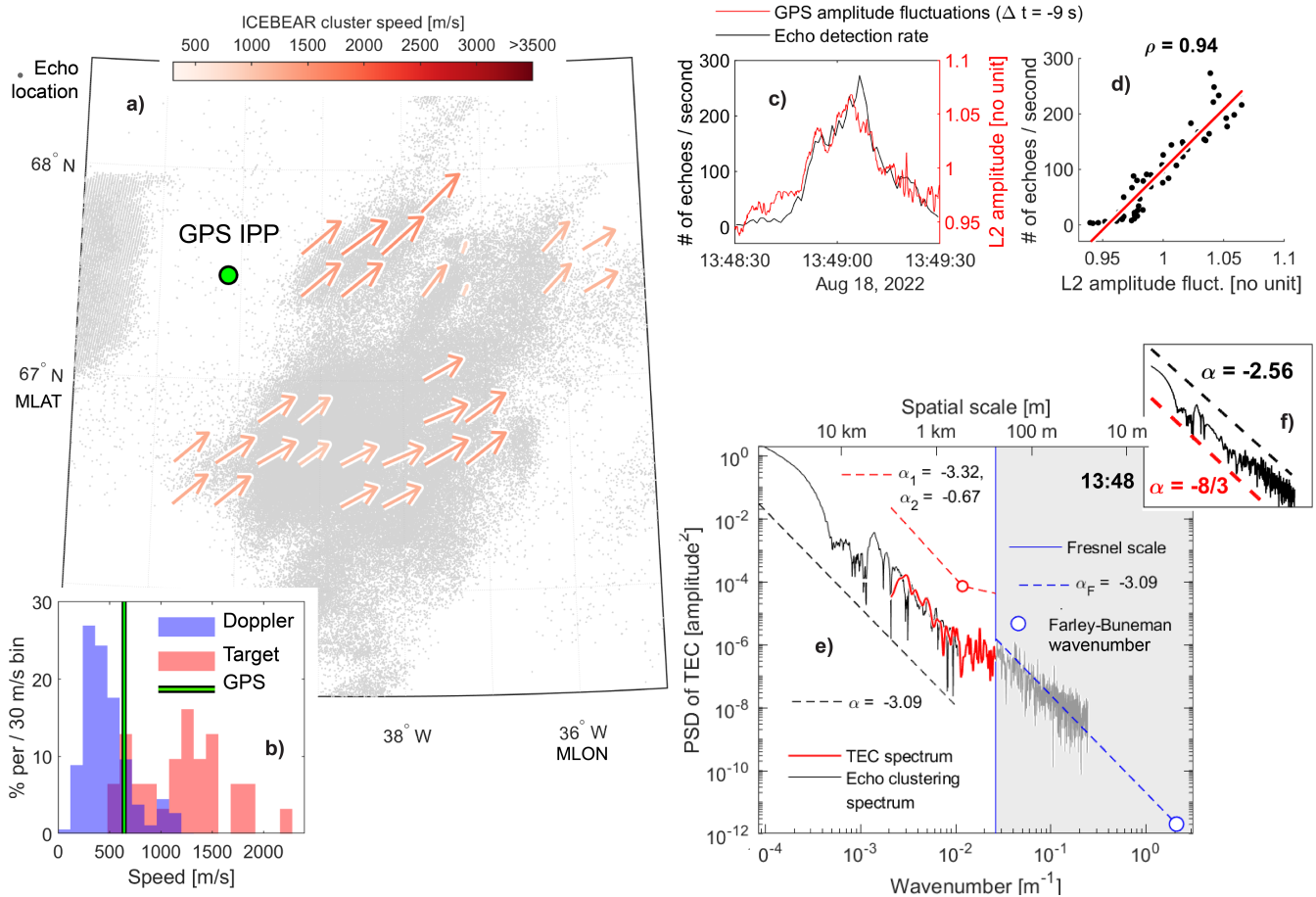


Figure 3. **Panel a)** shows the spatially averaged vector field of ICEBEAR target motions detected during the 15-minute interval starting on 13:45 UT on 18 August 2022, gray dots indicate echo locations, color-coded arrows denote the target motions, while a green circle indicates the position of a GPS pierce-point (IPP). **Panel b)** shows histograms for the Doppler speeds (blue) and echo cluster speeds (red), compared to the GPS phase screen velocity (green line). The next three panels detail a brief, two-minute conjunction event between ICEBEAR and CHAIN, with **Panel c)** showing the observed GPS amplitude fluctuations (red, right axis) with radar echo detection rates superposed (black), where we have applied a nine-second lag to align the two timeseries. **Panel d)** shows this data in a scatterplot, with Pearson correlation coefficient indicated, exhibiting a very strong correlation (Pearson coefficient $\rho = 0.94$). **Panel f)** shows the composite radar-GNSS spectrum, with spectral index calculations indicated. Inset **Panel f)** shows the overall spectral index fitted to the composite spectrum (black dashed line), compared to a theoretical kinetic Alfvén value of $-8/3$ (red dashed line).



echoes and the GPS amplitude fluctuations. Panel e) shows the composite spectrum, with detailed log-log linear fits of the two
185 spectra shown with black, red, and blue dashed lines. We observe the clear tendency for the two instruments to essentially
measure the very same structure from two different perspectives. Both the temporal (Figure 3c, d) and spatial (Figure 3e)
components agree remarkably well, confirming a clear common and immediate origin of the two multi-scale signals.

Next, we shall dissect an extended, one-hour conjunction, during which we observed three GPS amplitude scintillation
events [implying small-scale structuring (Song et al., 2023)]. Figure 4 shows the detailed observations made by ICEBEAR and
190 CHAIN, during which ICEBEAR detected and localized a staggering 2.3 million individual radar echoes (see Figure A1a–c for
the three composite radar-GNSS spectra calculated during this event).

Figure 4a) shows an overview of the observational volume, the ionospheric E-region, during the 20-minute interval 08:45–
09:05 UT, with the tracked ICEBEAR echo cluster motions shown with arrows demonstrating the fast and dynamic appearance
of radar aurorae; the tracked echo motions – the result of treating ICEBEAR as a tracking radar rather than a Doppler radar –
195 move through a GPS pierce point denoted with a green circle. The next panels in Figure 4 details the velocity observations
made by the two instruments during the full one-hour interval. Panel b) shows clearly that while the GPS phase drifts match
the observed radar Doppler speeds in an excellent fashion (average ~ 500 m/s), the observed target motions greatly exceed
those speeds (average ~ 1000 m/s). This is caused by the fact that the radar echoes' source regions being associated with
precipitation patterns (aurorae), move with the $\mathbf{E} \times \mathbf{B}$ drift of the F-region plasma (Ivarsen et al., 2024c, d, 2025b). However,
200 the Doppler speeds (and, very clearly also the GPS phase drifts) are limited to the ion acoustic speed, usually 400-600 m/s
(Foster and Erickson, 2000; Oppenheim and Dimant, 2013; Chau and St.-Maurice, 2016).

We were able to substantiate the foregoing using conjugate observations by the European Space Agency's Swarm satellites
(Friis-Christensen et al., 2006; Wood et al., 2022), a constellation that is in a polar orbit around Earth (inclination 87° , altitude
 $\sim 450 - 500$ km). Figure 5a) details a triple-conjunction between ICEBEAR, CHAIN, and two Swarm satellites. The latter
205 orbited through a region of active radar echo detection, and we observe that the radar echo cluster speeds agree very well with
the F-region ion drift speeds observed by Swarm A, in accordance with earlier conjunctions as well as statistical comparisons
(Ivarsen et al., 2024c, d). In addition, Figure 5b) shows that these speeds are greater than the GPS phase drifts

Following Ivarsen et al. (2023a) and Ivarsen et al. (2024a), we next Fourier analyze the Swarm 50 Hz magnetic field fluctu-
ations transformed into a mean-field-aligned coordinate system, yielding information on the field-aligned current structuring,
210 or, alternatively, current filamentation (Park et al., 2017; Ivarsen et al., 2020). The quantity is analogous to the structuring of
magnetic field-tubes in the plane perpendicular to the geomagnetic field. As the satellites orbit through the topside (F-region)
ionosphere with a velocity of $v_s = 7.62$ km/s, we apply Taylor's "frozen-in" assumption (Fredricks and Coroniti, 1976) to
convert the temporal FAC powerspectra to spatial k -spectra. These are superposed on the composite radar-GNSS spectra in
Figure 5c), showing good agreement on a wide range of spatial scales between 10^5 m and 750 m (below 750 m, the Swarm
215 spectra drop off, indicating an *effective* Nyquist frequency of 12.5 Hz for the Swarm magnetic field instrument). See Section B
in the Appendix for details of this triple conjunction.

We normalize the power amplitude between the various instruments to facilitate a direct spectral shape comparison, and we
apply an automatic spectral slope- & break-point detection algorithm based on piecewise linear Hermite polynomials (D'Errico,

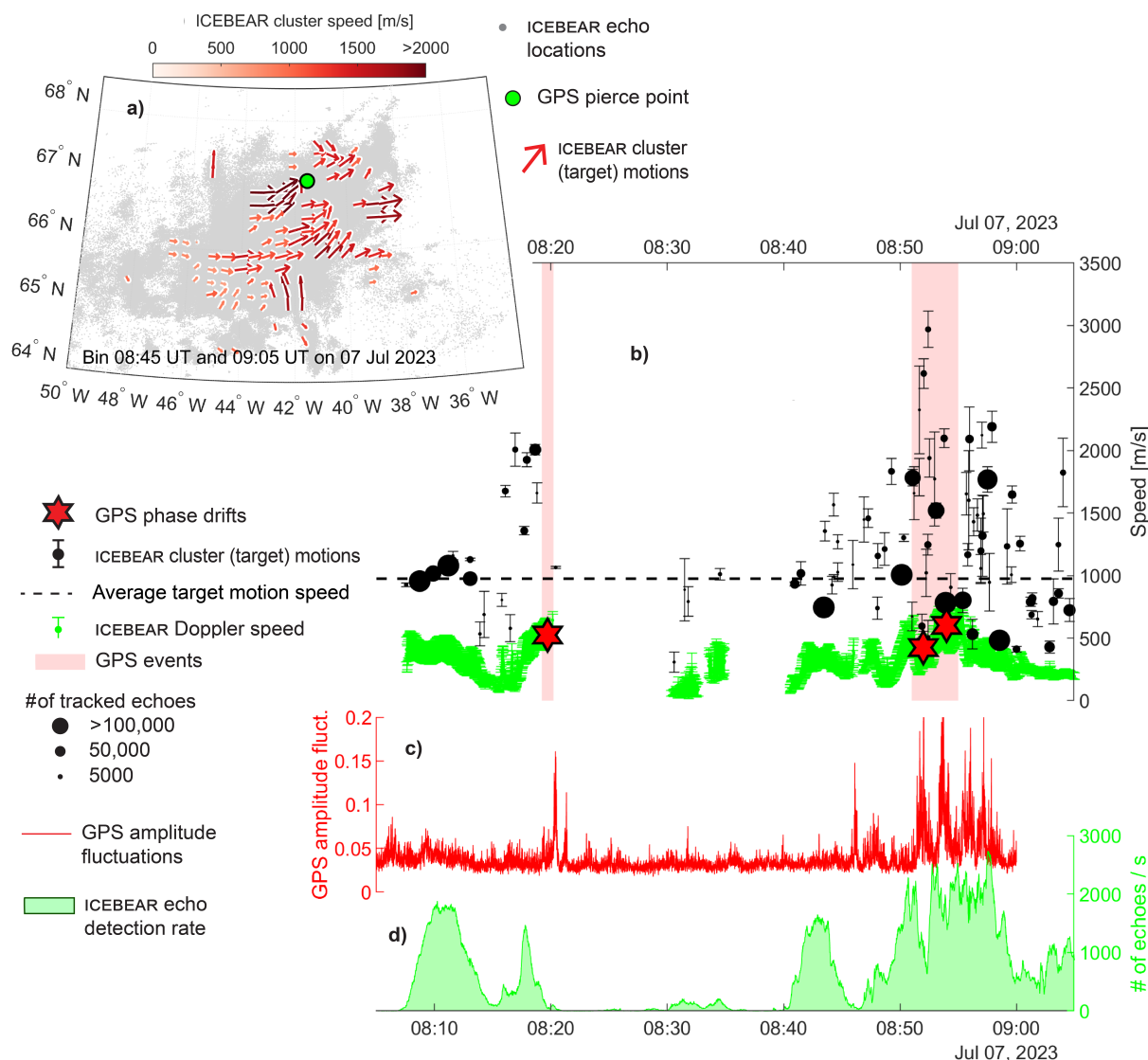


Figure 4. An extended conjunction between ICEBEAR and the CHAIN GPS receiver at Rabbit Lake in Saskatchewan, Canada, on 7 July 2023. **Panel a)** shows geospace over Rabbit Lake in geomagnetic coordinates, with the locations of 1.4 million radar echoes shown with grey dots, using the altitude-adjusted corrected geomagnetic coordinate system. Color- and size-coded arrows show the spatial average of the observed ICEBEAR cluster motions in the interval between 08:45 UT and 09:05 UT, while the location of the GPS pierce point is shown with a green circle (100 km altitude). **Panel b)** shows, for the one-hour interval between 08:05 UT and 09:05 UT, a timeseries of binned ICEBEAR echo cluster speeds (black, size-coded circles, with errorbars), ICEBEAR Doppler speeds (green dots with errorbars), and GPS phase drift speeds (red hexagrams). A black dashed line shows the average cluster speed. **Panel c)** shows fluctuation in recorded GPS signal amplitude (red axis), while **Panel d)** shows the rate of detected ICEBEAR echoes (green axis).

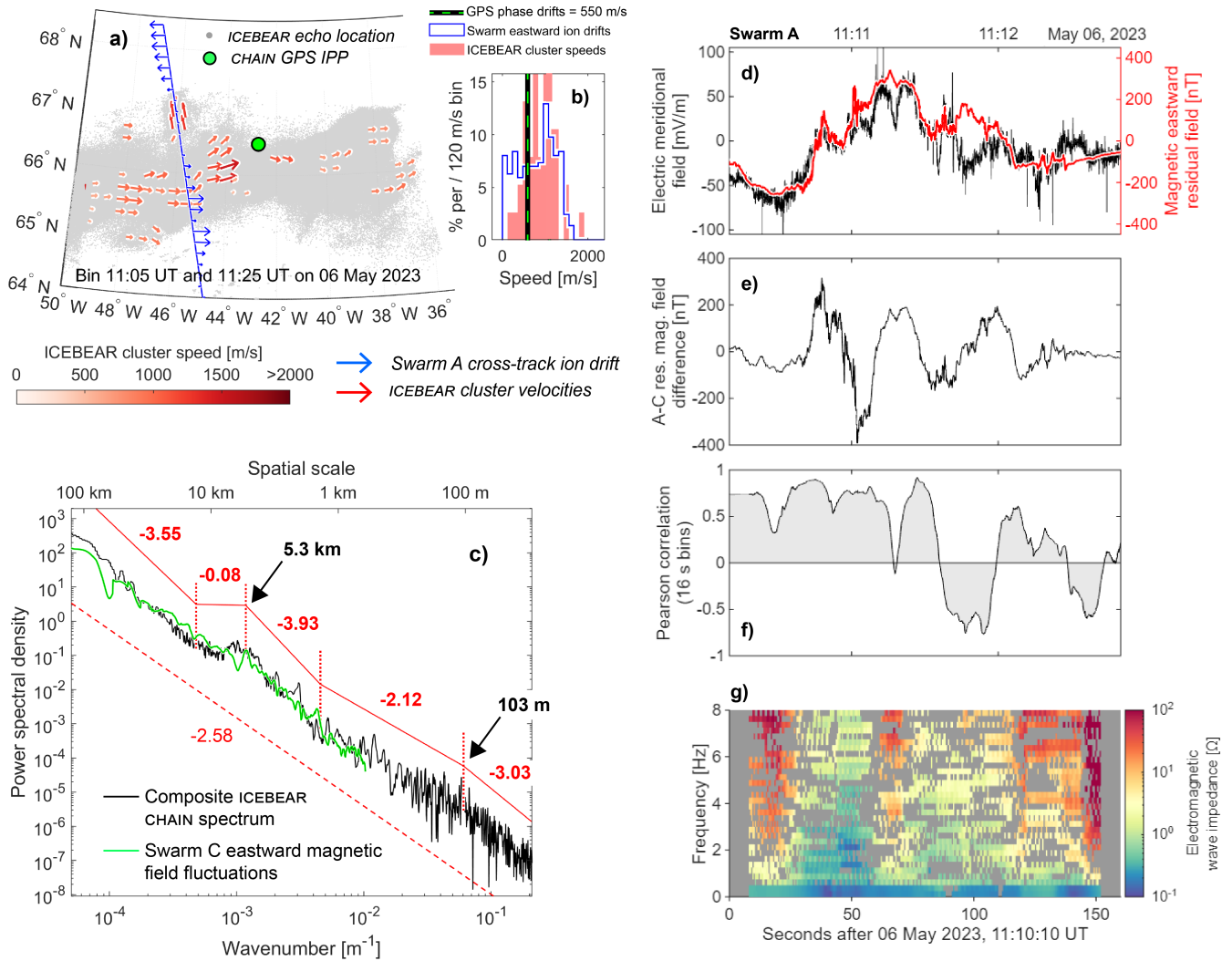


Figure 5. Panel a) shows the spatial distribution of radar echoes (grey point-cloud), the ICEBEAR echo cluster velocities (red arrows), the Swarm A cross-track ion velocities (blue arrows), and the ionospheric GNSS pierce point (green circle). Panel b) shows the observed GPS phase drift speed (black and green line), and distributions of the Swarm A cross-track ion drift magnitudes (blue line) and observed ICEBEAR echo cluster (target) motions (red shaded area). Panel c) shows the average composite spectrum for the five-minute interval starting at 11:06 UT on 6 May 2023 (Black line). The normalized spectrum of eastward magnetic fluctuations measured by Swarm C is shown with a green line. A five-component piecewise log-log linear fit is shown above the spectra (solid red line) while a single-slope fit is shown below the spectrum (dashed red line). Spectral indices and breakpoints are indicated in red and black lettering respectively. Panel d) superposes the meridional electric field component (black) with the eastward magnetic residual (red, right axis), panel e) shows the observed difference in magnetic residual field by Swarm A and C (shifted using a cross-correlation analysis), and panels f) and g) show the Pearson correlation and an impedance spectrogram respectively, both within running 16-s windows, and the latter in accordance with the decoherence masking method due to Pakhotin et al. (2018). See Figure B1 in the Appendix for additional details.

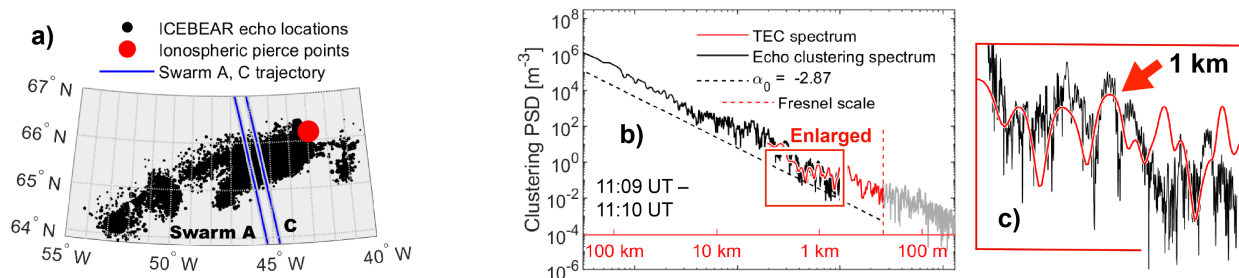


Figure 6. A triple conjunction between ICEBEAR, CHAIN and Swarm A, during a period more limited than that of Figure B1 Panel a) shows locations in geospace whereas panels b) and c) show the composite radar-GNSS spectrum. See Figure B1 in the Appendix A.

2009), with details described in, e.g., Ivarsen et al. (2019) and Ivarsen et al. (2021). For the overlapping scale-sizes between
 220 750 m and 3000 m, the spectral shapes are observed to match surprisingly well. The exponent of the fitted power laws, referred
 to as spectral index, tracks energy dissipation (Ivarsen et al., 2019), and we observe in Figure 5c) that the shape-wise agreement
 between the F-region FAC spectrum and the E-region radar-GNSS is excellent, echoing recent conjunctions of a similar nature
 (Ivarsen et al., 2023a, b, 2024a), and consistent with the filamentary nature of the field-aligned currents observed around diffuse
 aurorae (Gillies et al., 2015).

225 Meanwhile, using a Swarm-based electromagnetic wave impedance analysis due to Pakhotin et al. (2018), Figure 5d–g)
 demonstrates a clear Alfvénic signature at Swarm altitude. We deduce this from the, at times, strong (> 0.9) correlation in the
 transverse E-M components (Figure 5f) and the, at times, flat impedance spectra (Figure 5g). We therefore ascertain that Alfvén
 waves were actively threading the flux tubes connected to the E-region radar echoes. Seen together with (i) the overall spectral
 indices in Figure 5c) being close to the kinetic-Alfvén value of $-8/3$ (Boldyrev and Perez, 2012; David and Galtier, 2019), and
 230 (ii) the spectral shape of the composite radar-GNSS spectrum matches filaments in the aurorae very well (Figure 5c), we point
 to the likely Alfvénic origin for the echo point-cloud shapes.

Note that the observations reported in the present paper were performed during arctic summer, and were thus occurring in full
 daylight, except for the Figure 1 example. As such, we have no *optical* observations of the aurora to rely on; we do however note
 that ICEBEAR radar data is unequivocally and inexorably tied to the presence of aurorae (Ivarsen et al., 2024a, c, d, b, 2025a).
 235 In addition to this inference, we shall also demonstrate, during a data-rich conjunction study, that the source of our observed
 spectral density is, in fact, strongly linked with *auroral particle precipitation*, which by all intents and purposes *is* the aurora.

On 2 August 2023, an extended conjunction took place between ICEBEAR and the Japanese inner magnetosphere satellite
 Arase. During this conjunction, two additional ICEBEAR–CHAIN conjunctions took place. What follows is an analysis of the
 detected, *in-situ* electron flux observed by Arase during that conjunction, compared to the spectral density observations by our
 240 ground-based instruments.

Arase orbits Earth at a maximum distance (semi-major axis) of around 5 Earth radii, with a magnetospheric orbit that keeps
 the satellite relatively close to equator with an ionospheric footprint that routinely sample auroral latitudes (Miyoshi et al.,
 2018b, 2022): it has an apogee of 32,000 km and a perigee of 400 km, an inclination angle of 31° , and a period of 570 minutes.

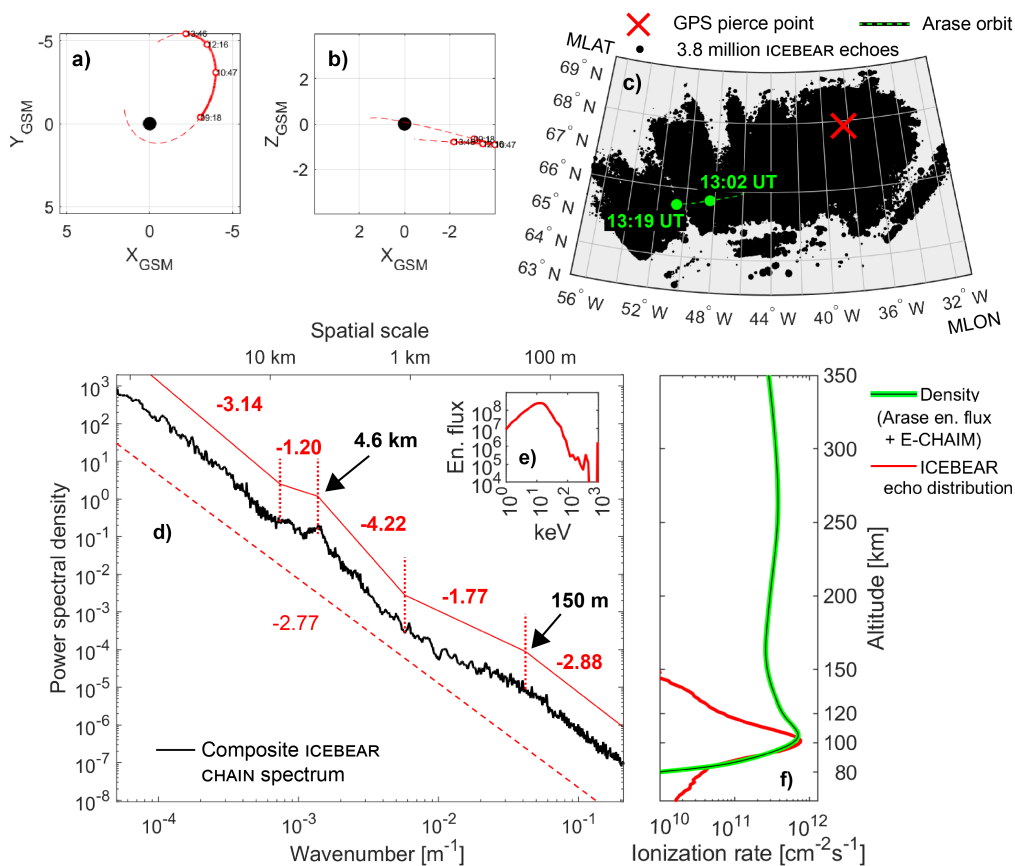


Figure 7. A space-ground-ground conjunction between ICEBEAR, CHAIN, and the Japanese inner magnetosphere spacecraft Arase that took place on 2 August 2023. **Panel a, b)** show the satellite location in the magnetosphere, in units of Earth radii, the black dot at the center being Earth itself. **Panel c)** shows the geospatial distribution of radar echoes in the E-region (black), with Arase’s northern hemisphere ionospheric footprint plotted with green dashed lines [using the Tsy04 mapping method (Tsyganenko and Sitnov, 2005)], and the GPS pierce-point as a red cross, all in the field-line adjusted AACGM coordinate system (Baker and Wing, 1989). **Panel d)** shows the composite ICEBEAR-CHAIN spectrum measured during the 17-minute interval starting at 13:02 UT on 2 August 2023. **Panel e)** shows the average precipitating electron spectrum measured by Arase during the interval, combining the low (LEP-e), medium (MEP-e), and high (HEP) energy particle detectors (Kazama et al., 2017; Kasahara et al., 2018; Mitani et al., 2018), and using pitch angles lower than 5° (LEP-e, MEP-e) and 10° (HEP). **Panel f)** shows, in red, the altitude distribution of ICEBEAR echoes and, in green, the plasma density altitude profile created by the precipitating particles measured by Arase using the E-CHAIM model (Themens et al., 2017) to incorporate the effects of solar extreme-ultraviolet photoionization.

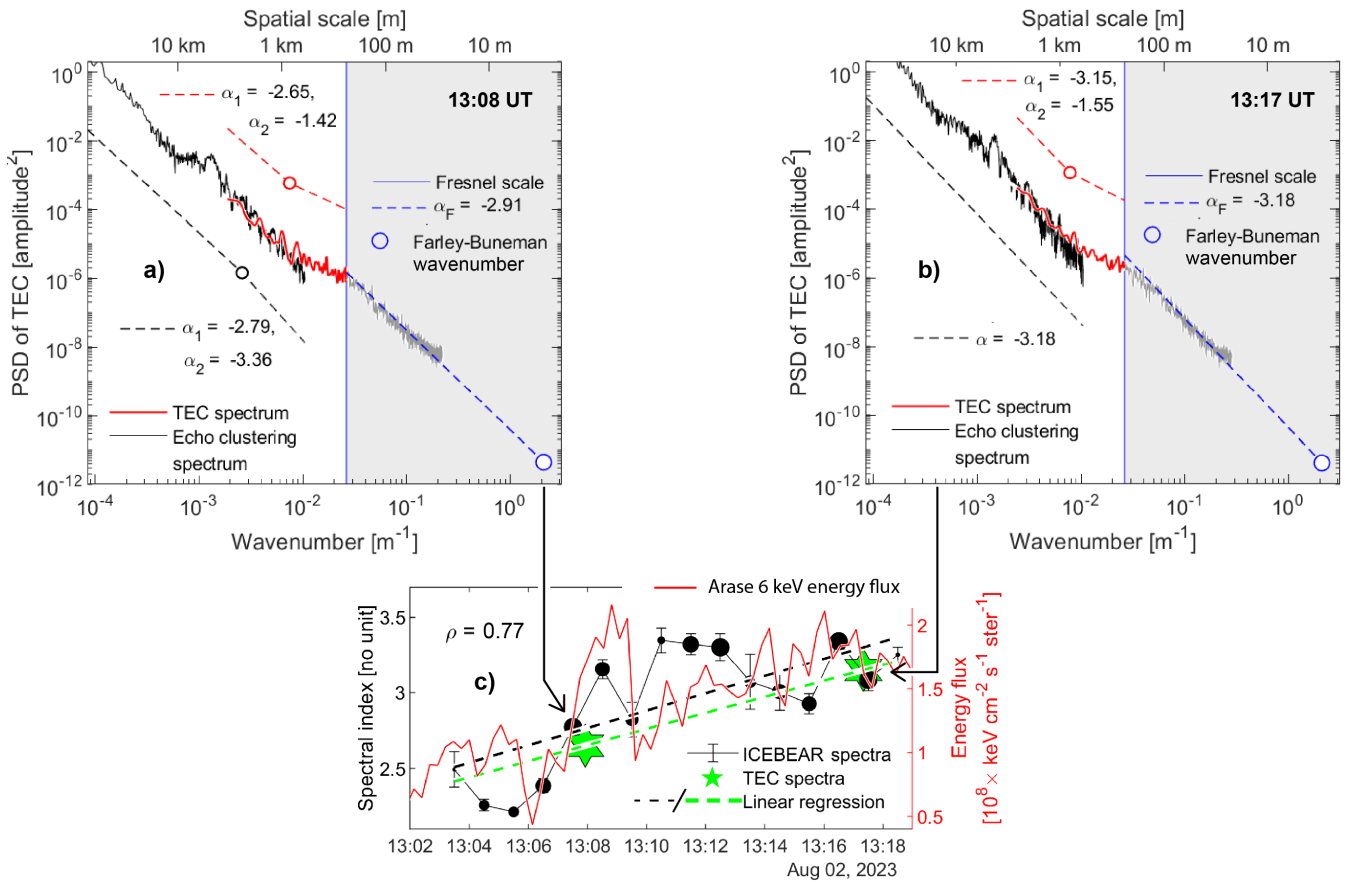


Figure 8. Panels a) and b) show two composite spectra, where the ICEBEAR clustering spectrum is shown in black and the TEC spectrum is shown in red and dark grey. A log-log two-component piecewise fit is shown for both spectra, as well as a linear fit for the TEC spectrum below the Fresnel-scale; spectral indices are indicated. Panel c) shows a timeseries of spectral index values, comparing α_1 from ICEBEAR (before the possibly noisy fall-off near 1 km), with α_1 from the CHAIN GNSS spectra. Some 100 ICEBEAR spectra observed during the interval 13:02 UT–13:19 UT are binned in one-minute bins, and are shown with black circles (with errorbars denoting the variability inside each bin) and α_1 from the two CHAIN TEC spectra are shown with green hexagams. On the right axis we show the observed low-pitch angle ($\leq 5^\circ$) flux of electrons measured in the 6 keV channel of the low-energy particle detector onboard Arase, selected for its high correlation with the spectral timeseries; ' ρ ' indicates Pearson correlation at zero lag (see Figure 7 for details of the Arase conjunction).



The satellite's magnetospheric location and ionospheric footprint during the conjunction are shown in Figure 7a–c), and we use
245 the Tsy04 model for tracing the location of the satellite along Earth's field-lines (Tsyganenko and Sitnov, 2005). The satellite
was located some 19° raised above magnetospheric equator, while observing a considerable flux of electrons with low pitch
angles. Figure 7e) shows the particle observations, showing the total measured electron flux with low pitch-angles (close to 0°),
for an extended period during which the satellite continuously orbited through regions mapping to regions of rather extreme
E-region echo activity (Figure 7c). The satellite likewise observed some upper-band chorus waves (not shown), and we infer
250 that the observed flux of low-pitch-angle particles is a proxy of the real precipitating particle flux, producing the characteristic
diffuse aurora that we infer for this event.

The observed number flux relates to an energy flux (Redmon et al., 2017), which is readily converted to ionization rate
altitude profiles (Fang et al., 2010), and we use the E-CHAIM model to convert this into a plasma density profile (Themens
et al., 2017). In Figure 7f) we compare the estimated density profile (green line) with the measured altitude distribution of the
255 observed radar echoes (red distribution).

During the 17-minute interval, ICEBEAR observed almost *4 million* individual echo locations, which we cluster using the
Monte-Carlo model described in Section 2. Some 100 clustering spectra were calculated during this interval, and Figure 7d)
plots the composite ICEBEAR-CHAIN spectrum for the entire interval.

Figure 8 plots, with black circles, 1-minute binned spectral index measurements, taking the initial ICEBEAR spectral index
260 (the slope *before* the near-resolution fall-off), and comparing this to the initial CHAIN spectral index. This spectral interval
goes over the injection wavelength or knee at ~ 5 km and provides a reasonably representative index of the larger wavenumber
interval. In addition, in green hexagrams, we show the initial (overlapping) slope of the ISMR TEC spectra. A linear regression
is applied to the spectral index results from the density curves. We note that the locations of both hexagrams are in excellent
agreement with the spectral index results. This being stated, we also note, that the event appears to have been a “two-plateau
265 event” with a spectral index of -2.3 prior to 13:08 where the impinging fluxes were weaker and another value of -3.2 afterwards,
following a marked increase in precipitation flux. The important point here is that there is a clear increase in slope magnitude
(steepening spectra) in Figure 7g) that goes together with the unequivocal increase in the observed precipitating energy flux
represented by the flux through the 6 keV channel of the MEP-e instrument (red line in Figure 7g).

So far, we have shown the case for the spectral density comparisons (Figures 5c and 7g) where the observed spectra are
270 *consistently steep*, for all wavenumbers except for prominent transitions near 5 km and near the Fresnel-scale around 270 m.
Based on Figure B1 as well, we ascertain, with some confidence, that these observed structures are *contained* within filamentary
field-aligned currents that are carried by the precipitating particles. (Ivarsen et al., 2023a, 2024a).

Added support for the foregoing narrative was also obtained from a separate statistical analysis gathered from two years of
data. That is to say, the overall steepness of the spectra that we have just discussed have been routinely found when filamentary
275 FAC are present. To be specific, the inferences made from the 10 ICEBEAR CHAIN conjunctions are backed in Figure 9a) by
the index distribution of 7,700 ICEBEAR clustering spectra observed during the two years 2020, 2021 [the same database that
was used in Ivarsen et al. (2023b)]. In Figure 9a), this distribution is shown with a dark red line, and its shape and mode (peak)



agree with the foregoing, namely, we observe a consistently steep spectral shape with the most probable spectral index being close to $-8/3$.

280 Thus, Figure 9 clearly demonstrates a consistent tendency for a value around $-8/3$ as the most probable measurement value overall, and a relatively narrow spread around that value. The echo altitude distribution is also shown for the 10 events in Figure 9d) peaks at 102 km. Using this altitude for the GPS pierce points gives us a phase screen drift of around 500 m/s, coinciding with the peak of the median Doppler speed distribution for the 10 events (Figure 9b). As discussed above the only reasonable explanation for this signature is that those structures are Farley-Buneman waves that reach their largest
285 amplitudes at the ion acoustic speed, just as is observed in HF and VHF radars. This important observation confirms that the GPS scintillations not only took place in the E-region, a notion supported by recent statistical studies (Blinstrubas et al., 2025), but that they were also caused by long-wavelength (270 m) Farley-Buneman turbulence.

4 Discussion

There are two prominent and, to a certain extent, unexpected results in the present study. First, the observed radar Doppler
290 speeds agree remarkably well with the GPS phase drifts, while being clearly much smaller than the tracked echo motions. The second prominent result is the seemingly universally steep power spectra that we observe with ICEBEAR and CHAIN. We shall now discuss these points in order.

4.1 Long-wavelength Farley-Buneman waves and their fate

As has been repeatedly pointed out in references cited above, the Doppler speeds extracted from VHF radars in the auroral
295 electrojet typically do not exceed the E-region ion acoustic speed, with due exceptions associated with narrow spectra extracted from the edge of the instability cone in the upper part of the unstable E-region (St-Maurice et al., 2023). This being stated, the E-region cluster motions extracted from ICEBEAR as a target radar are clearly much faster than the ion-acoustic speed when the electric field is very strong. The target motions correspond to the motion of magnetic field tubes drifting at the $\mathbf{E} \times \mathbf{B}$ -drift while said field tubes are exciting large-amplitude ion-acoustic waves for a brief moment during which the electric field locally
300 must go down to the Farley-Buneman threshold value (Foster and Erickson, 2000; Oppenheim and Dimant, 2013; St.-Maurice and Hamza, 2001). Thus, the sources of the ion-acoustic waves are moving at a drift that matches the F-region plasma drifts. This feature has been exemplified in Figure 5a, b), and in recent literature on the subject (Ivarsen et al., 2024c, d).

We have to consider the fact that the Fresnel-scale (~ 270 m) structures also exhibit GPS phase drifts moving at the ion acoustic speed rather than at the $\mathbf{E} \times \mathbf{B}$ -drift. Gradient-drift waves are not constrained by the ion-acoustic speed. Even if, like
305 the smaller m-size structures, they were to grow to an amplitude such as to reach threshold conditions, the balance would involve chemistry and diffusion, not ion inertia and diffusion. However, since the 270 m waves move at the ion-acoustic speed when their amplitude is the largest (which is what we observe), the simplest explanation for this result is that the observed Fresnel-scale structures are, in fact, controlled by ion-inertia, i.e. they are *Farley-Buneman (FB) waves*. However, according to the standard linear fluid theory for altitudes between 100 and 105 km, the growth rates expected are 10,000 times smaller

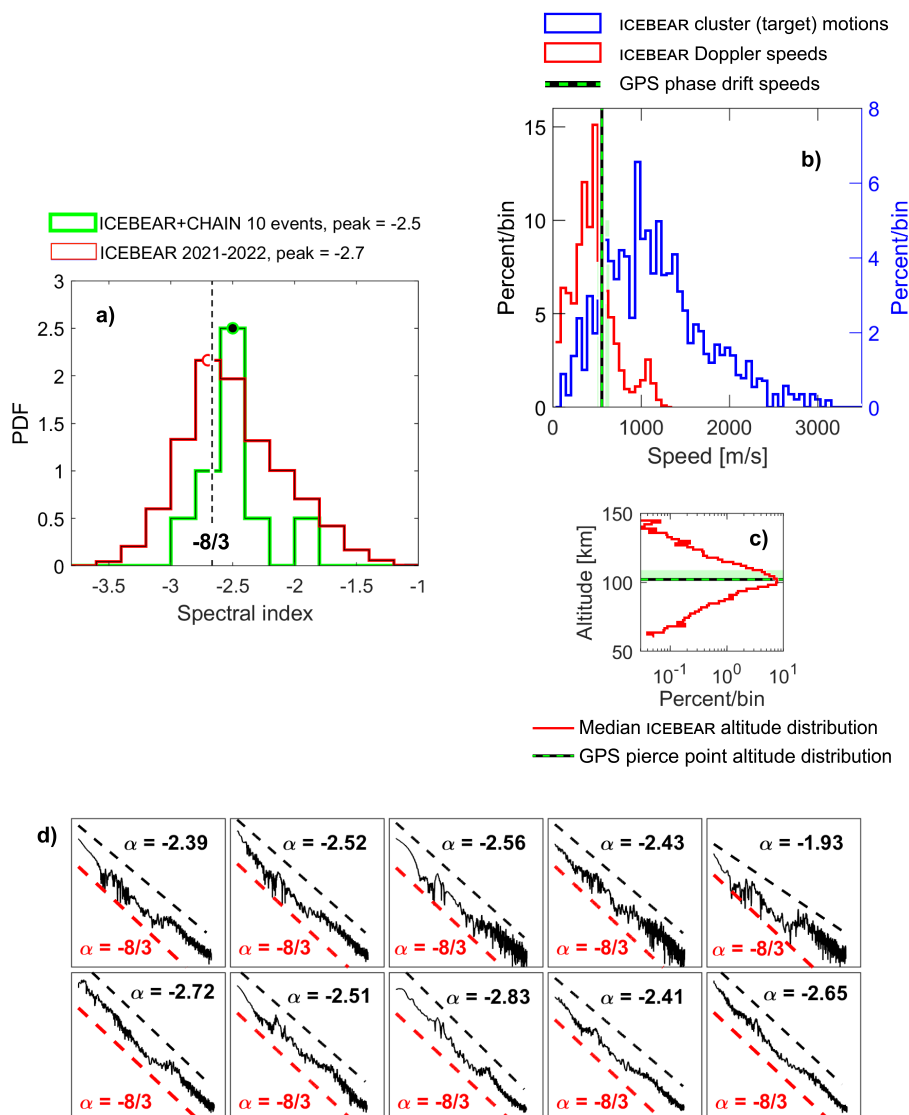


Figure 9. **Panel a)** compares the ICEBEAR-CHAIN spectra (green line) with a statistical aggregate of 7,700 ICEBEAR echo clustering spectra (red line) observed during 2020, 2021 [the database that was analyzed in Ivarsen et al. (2023b)]. **Panel b)** shows the mean distributions in VHF radar Doppler speeds (red histogram), the mean distribution in observed echo cluster (target) motion (blue histogram), and the average GPS phase drift speed (green and black line). **Panel c)** shows the distribution of echo altitudes, with a black-and-green line indicating the assumed GPS pierce-point locations (with shaded green region giving upper/lower quartile distributions). **Panel d)** shows all 10 composite ICEBEAR-CHAIN spectra (solid black line), with a linear log-log fit (black dashed line) and a $-8/3$ -slope (red dashed line) indicated.



310 at 270 m than at 2.7 m. That is to say, the growth rates are given by $Ck^2(Vd^2 - C_s^2)$ where C is a well-known constant, V_d
is the relative drift between ions and electrons (basically E/B at those altitudes) and C_s is the ion-acoustic speed (Fejer and
Kelley, 1980). The k^2 dependence can be compensated to a certain extent if the electric field is itself ~ 10 times stronger than
the threshold value (200 mV/m as opposed to 20 mV/m). In that case, the growth rate picks up by a factor of 100 and the
factor 10,000 is down to a factor 100 compared to the growth rate of meter-size FB waves probed by radars under ordinary
315 electric field conditions. Put in another way, in spite of weaker growth rates, it might be feasible to excite FB waves at a couple
of hundred meters, particularly when the electric fields are *strong*. This being stated, ? have seen evidence in their numerical
simulations for nonlinear 160 m structures growing at a much faster rate than expected from linear theory. They attributed the
growth to an energy extraction from the smaller scale FB waves, i.e., to what could be described as a reversed, or inverse,
cascading process.

320 Still, the fact, that the *FB waves* are observed to move at the ion-acoustic speed, requires a comment in view of seeing
270 m-sized waves move at that speed. First of all, a high-resolution Continuous Wave (CW) experiment has shown that FB
waves are at first moving much faster than at the ion-acoustic speed, but that as their amplitude grows they reach a much larger
amplitude at the ion-acoustic speed after which they simply disappear quickly (Prikryl et al., 1988, 1990). This means that
the meter-size FB waves follow linear theory expectations at first but that as they grow in amplitude, they reach a maximum
325 amplitude at the ion-acoustic speed, after which they quickly disappear. Radars are biased to the largest amplitude structures
and therefore see them moving at the ion-acoustic speed (or slower depending on the line-of-sight). We note that one may wish
to use the word "threshold speed" instead of "ion-acoustic speed." In particular, electron heating perturbation effects modify
the threshold speed below 100 km altitude and ion heating perturbations would also matter above 110 km [see St.-Maurice and
Chau (2016) for a comprehensive review of the situation]. Given that the observations presented here are mostly from the 100
330 to 105 km altitude region, the threshold speed and the ion-acoustic speed are very close to being one and the same.

Numerical simulations have indeed found that the largest amplitude waves move at the ion-acoustic speed in a direction
roughly matching the ExB direction (Dimant and Sudan, 1995). Theoretical work has involved anomalous diffusion (Robinson,
1986), mode-coupling explanations, for example in Hamza and St-Maurice (1993) & references therein, and double polariza-
tion effects, as per the work by Sato (1972) and St.-Maurice and Hamza (2001). These notions all use the fact, in one way or
335 the other, that the unstable situation introduces a polarization electric field that moves electrons *against* the original electric
field direction, thereby damping the electron fluid. This is a wave-particle interaction that affects the nature of the local energy
expenditure. For instance, Sato (1972) and St.-Maurice and Hamza (2001) used a relatively simple approach by considering
structures that, while initially elongated, were not ideal plane waves. The two-dimensionality leads to a decrease in the electric
field inside the waves as the wave grows. We note the circularity in this situation, as the electric field evidently works to move
340 charges, but at the same time also extinguishes itself, which weakens local charge motion. The rapid feedback stops when the
electric field is at threshold conditions. This is what saturates a Farley-Buneman wavefield, and the work done in causing this
saturation is substantial.

On that note, the FB waves also have a nonlocal character, as their eigenfrequency is a small but non-negligible function
of altitude, i.e. of position along the geomagnetic field (Drexler et al., 2002). This introduces vertical shears that short-out



345 the electrostatic fields and dissipate the waves while heating the electrons (Maynard et al., 1973; Vickrey and Kelley, 1982;
St-Maurice and Goodwin, 2021; Zhang and Varney, 2024; Ivarsen, 2026). In this light, even if the growth rate of 270 m waves
is from an inverse cascading process, a final nonlinear evolution has to limit the growth through the kind of mode-coupling or
double polarization effects described above, since the principle applies to initial elongated structures of any width or size. As
a result, 270 m structures at 102 km end up at the ion-acoustic speed as long as they are the byproduct of the FB instability, be
350 it through linear or nonlinear growth processes.

4.2 Universally steep power spectra in filamentary FAC regions

Every time we had FAC data from satellites, the steep spectral slopes with indices of about $-8/3$ were observed in diffuse auroral
regions and intense filamentary FAC structures. This is not surprising, since current filaments are associated with Alfvén waves,
and the mode of the spectral slopes (not its spread) confirm this fact. We need to stress that not all the events were associated
355 with slopes and with FAC filaments, which is consistent with a minority of cases for which the spectral slope was clearly not
so steep (as seen with minor but real deviations from the overall statistics in Figures 9a and 8c above). The fact remains that
a vast majority of cases were associated with filamentary FAC and Alfvén waves. This underscores an important fact: while
not quite all spectra had a $-8/3$ spectral index, when they did, the spectral slope extended to all scales available to our scrutiny,
down to 20 m.

360 We already know that Alfvén waves were involved in the observed filamentary parallel current regions (Figure B1), and the
associated power spectrum has a $-8/3$ spectral power index. This wave spectrum has been associated with kinetic magneto-
hydrodynamic (MHD) turbulence, in particular kinetic Alfvén waves (KAWs), (Boldyrev and Perez, 2012; Chen et al., 2013;
Galtier and Meyrand, 2015; David and Galtier, 2019). Those waves are generated in the warm magnetospheric plasma. They
propagate into the cold collisional ionosphere, where they transition into inertial or dispersive Alfvén waves, in the process,
365 preserving the spatial scaling of the driver. The waves are reflected back or are absorbed by the plasma. This modulates the
local electric field. As we have reported here, in the E-region, these structured electric fields instantly trigger turbulent dissipa-
tion, notably through the Gradient-Drift Instability (GDI) and the FB. The question to ask is: how is it that in spite of the clear
presence of abundant FB waves (as observed by ICEBEAR) the spectrum keeps a distinct $-8/3$ Alfvén wave signature for all
scales available to our scrutiny, that is, down to at least 20 m, long past the 270 m mark where FB waves are evidently causing
370 the structure?

Consistent with the notion of a trigger of ionospheric plasma instabilities, we note that the steep spectra are interrupted by
two knee regions, one near 5 km wavelength and the other near 200 m. Injection wavelengths of the order of 5 km are typical
of scales associated with the largest Gradient-Drift (GD) waves found in the equatorial electrojet region. At the equator, they
are triggered by electric fields of the order of 15 mV/m or greater in combination with vertical density gradient scales of the
375 order of 10 km (Tsunoda et al., 1982). Somewhat larger size GD waves are possible, but at some point their growth is limited
by chemical recombination when the latter becomes faster than the gradient contribution to the growth rate. We note that, in
the equatorial regions, GD waves can modulate small scale FB waves if the ambient electric field exceeds 15 mV/m. Also,
GD waves have been proposed as a seed for FB waves: as unstable fingers associated with GD structures move into increasing



low density regions, the gradients on their side could steepen to the point that the instability threshold of FB waves is achieved
380 (Sudan et al., 1973).

The other knee at 200-300 m seems to be associated with the Fresnel size of structures seen near 102 km. We found, unexpectedly, that those waves are FB waves in spite of their large size, i.e., of their weak linear growth rates. However, since the growth rate may be linked to nonlinear “inverse cascading”, it is tempting to assume that this match between the knee and the Fresnel FB structure is not a coincidence and that this describes the largest FB waves in the system. However, the GPS
385 events analyzed in this paper were selected for exhibiting strong amplitude scintillations, and so there is likely a selection effect favouring Fresnel-scale energy injection events.

A third component of the puzzle is the density of FB irregularity bursts monitored by ICEBEAR. As stated in a preceding section, FB waves are ephemeral and can come and go in a fraction of 1 s. Both theoretical and numerical works indicate that the maximum amplitude of these waves is not increasing dramatically with electric field strength. Instead, what increases is the
390 abundance of the FB waves. This is not intuitively difficult to understand since stronger electric fields mean faster linear growth rates, meaning more growth events per unit time, meaning more growth episodes per unit space. The growth in the number of large amplitude scatterers has in fact been demonstrated in spectacular fashion in the work of Ivarsen et al. (2025a) who found the density of large amplitude ICEBEAR radar echoes to simply be proportional to the electric field when such field exceeded 40 mV/m ($E/B > 800$ m/s),

395 A final aspect to keep in mind is that FB waves are very efficient at extracting energy from Hall currents and giving it back to particles. This is not Joule heating *per se*, as it involves extracting kinetic and potential electric energy from the currents which then turns into a quick dissipation involving the creation by nonlocal processes of wave parallel electric fields and currents carried by electrons, which then give the energy gained from the resulting acceleration to the background gas through elastic and, mostly, inelastic collisions (see Section 4.1).

400 We arrive at the conclusion that powerful Alfvén waves transfer an unusual amount of their energy to FB waves by creating larger FB structures (which always have more energy than smaller structures) and by creating a number of such structures that increases proportionally to the electric field imposed by Alfvén waves, and, more generally, ULF waves [see Shen et al. (2024); Ivarsen et al. (2025a), as well as the present study’s own companion paper]. As a result of this increase in dissipation rate through unstable transient ionospheric structures, the Alfvén wave spectrum is able to keep its $-8/3$ spectral index. In other
405 words, the ionospheric structures are in lock-step with the Alfvén wave spectrum.

While there is clearly a need for future quantification, it remains an observational fact that the large-scale organization that emerges from packing thousands or millions of FB waves inside a limited volume is universally steep across four orders of magnitude in scale-size. We suggest here that incoming Alfvén waves are modulating the local electric field, on all scale-sizes, akin to the argument constructed by Ivarsen et al. (2024a). The “pre-structured” injections drive instabilities, and the fastest
410 evolving instabilities (FB waves) are used to maximize the energy extraction from Alfvén waves. The bursty nature of the FB structures actually helps maximize the rate of energy extraction and transfer it to the ambient gas.

The notion that Alfvén waves are directly structuring the E-region yields immediate explanatory power for the magnetosphere-ionosphere coupling. The coupled system would evolve toward a state of maximum energy dissipation, governed by Alfvénic



impedance matching and wave reflection: Particle precipitation that fails to reach the altitude with the lowest instability thresh-
old (St-Maurice et al., 2023) may cause impedance mismatch for the incoming Alfvén waves, causing Alfvénic power to be
reflected rather than dissipated. Consequently, the coupled system selectively sustains, and favours, precipitating electrons
whose emission profile peak at altitudes around 105 km where the FB instability threshold is lowest, offering a thermodynamic
explanation for the preferred altitude of pulsating auroras (Hosokawa and Ogawa, 2015; Partamies et al., 2017; Dahlgren et al.,
2017; Kawamura et al., 2020; Tesema et al., 2020; Nishimura et al., 2020). What is more, non-linear wave heating in the
upper part of the unstable layer suppresses dissociative recombination rates ($\propto T_e^{-1/2}$, Schlegel, 1988). It may even be that
the subsequent net increase in conductance may provide a significant contribution to the problem of the “saturating polar cap
potential” (see, e.g., Siscoe et al., 2004). In this regard, Section B presents observations from Swarm that indicate the satellite
in fact observed Alfvén waves that were absorbed without reflection, which is, incidentally, the most efficient way to dissipate
electromagnetic energy in our atmosphere.

We further speculate that the consistently steep $-8/3$ can be described in terms of a self-organized criticality, in which the
dissipation performed via Alfvén waves is locked or saturated against FB waves. This eventuality needs further scrutiny, and,
in a companion paper, we follow the notion to a logical conclusion, through the lens of the renormalization group, a device
intimately suitable for the topic of space weather model “sub-grid” parameterization.

5 Conclusion

Using a novel measurement technique, we have resolved the power spectral density of the E-region ionosphere across four
orders of magnitude in spatial scale. We found that in filamentary upward field-aligned current regions, the auroral plasma
preserves the structure of its magnetospheric driver, exhibiting the characteristic $k^{-8/3}$ scaling of kinetic Alfvén turbulence.
We also found that the 270 m structures associated with Fresnel scales in GPS scintillations were drifting at the ion-acoustic
speed. This was made very clear; for our samples, the GPS-inferred drift not only matched the expected value for the ion-
acoustic speed, but it was also much smaller than the plasma $\mathbf{E} \times \mathbf{B}$ drift inferred from the ICEBEAR target motions in the same
region (see Figures 4b and 9b). This means that the 270 m structures (which matched the position of a knee structure in the
overall spectrum) were actually Farley-Buneman waves, just like the much smaller scale 3-m waves detected by the ICEBEAR
radar. Since the FB growth rate at 270 m should be very small, this observation came as a surprise. The observation seems,
however, to confirm results from numerical simulations that found that large scale FB waves were excited nonlinearly through
an *inverse cascade* (?). The presence of such large-scale FB waves means that there can be far more energy dissipated by FB
waves than if only less than 10-m structures had been destabilized.

In closing, we note that the ionosphere’s bottomside, the E-region, has been ascribed many roles. In-situ satellite observations
not being possible we were left with short-lived rocket campaigns and a handful of incoherent scatter radars and only somewhat
more numerous coherent radars (Palmroth et al., 2021). Still the technology has become sophisticated enough to add, over time,
several new perspectives and insights. In the process the E-region has become more than just a region to pass Pedersen currents
that offer a closing of the magnetosphere-ionosphere current system, with attendant Joule heating and precipitating particle



energy dissipation rates. While these features are very important, the addition of fast temporal and much finer spatial resolution than before by ground-based instruments is producing a much more complex picture. We have highlighted a few of the new capabilities in the present paper, to which could be added many important results from incoherent scatter radar showing how dynamical the E-region can be (e.g., St-Maurice et al., 1990; Blinstrubas et al., 2025). The present study has continued the march towards new important insights by advancing our understanding of auroral plasma turbulence, with the new extraction of the composite radar–GNSS power spectrum.



Appendix: Geospace conjunction studies

This Appendix supports the findings presented in the main text, by providing technical, theoretical, and observational details
455 concerning the many multi-instrumental conjunctions that we analyze.

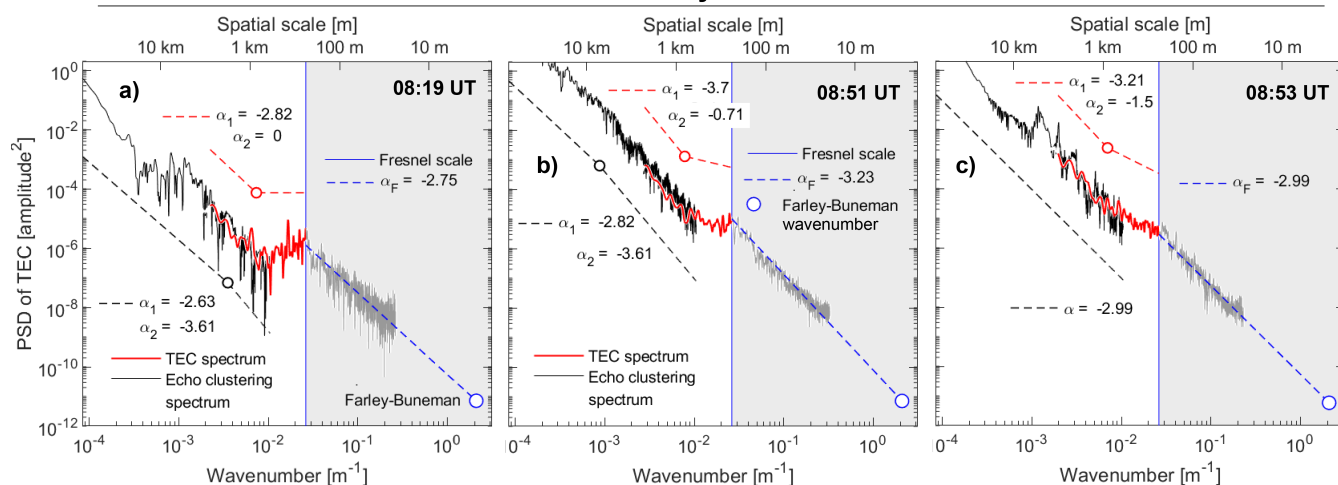
The Appendix is organized as follows. Section A (Figure A1) describes the core dataset used in the Main Paper, namely the ten ground-ground conjunctions between the experimental VHF radar ICEBEAR and the Rabbit Lake GPS receiver in the CHAIN network of ionospheric scintillation monitoring receivers (ISMRs). Section B (Figure B1) describes an extended space-ground-ground conjunction between ICEBEAR, CHAIN, and two European Swarm satellites.

460 Appendix A: Ten ICEBEAR-CHAIN conjunctions

Figure A1 showcases six simultaneous ICEBEAR-CHAIN conjunctions, occurring in rapid succession during two extended events that took place on 7 July 2023 and 18 August 2022. Each panel of Figure A1 shows the composite power spectrum for each conjunction event. We normalize the power amplitude to facilitate a direct spectral shape comparison, and we apply an automatic spectral slope- & break-point detection algorithm based on piecewise linear Hermite polynomials (D'Errico, 2009),
465 with close details described in, e.g. Ivarsen et al. (2019), and Ivarsen et al. (2021). For scale-sizes between 750 m and 3000 m the spectral shapes from the two different methods are observed to match strikingly well. What is more, the steep slopes at the larger scales (> 1 km) are highly consistent with the steep slopes seen at smaller scales (< 100 m), with observed spectral index values between -2.6 and -3.1 . A prominent break-point is observed near the Fresnel-scale, and similar prominent features are visible at scale-sizes around 1–10 km, both in accordance with expectations based on plasma instabilities from the literature
470 (Villain et al., 1986; Ivarsen et al., 2023b; Basu et al., 1990; Mounir et al., 1991; Spicher et al., 2014; Hamza et al., 2023).



7 July 2023



18 August 2022

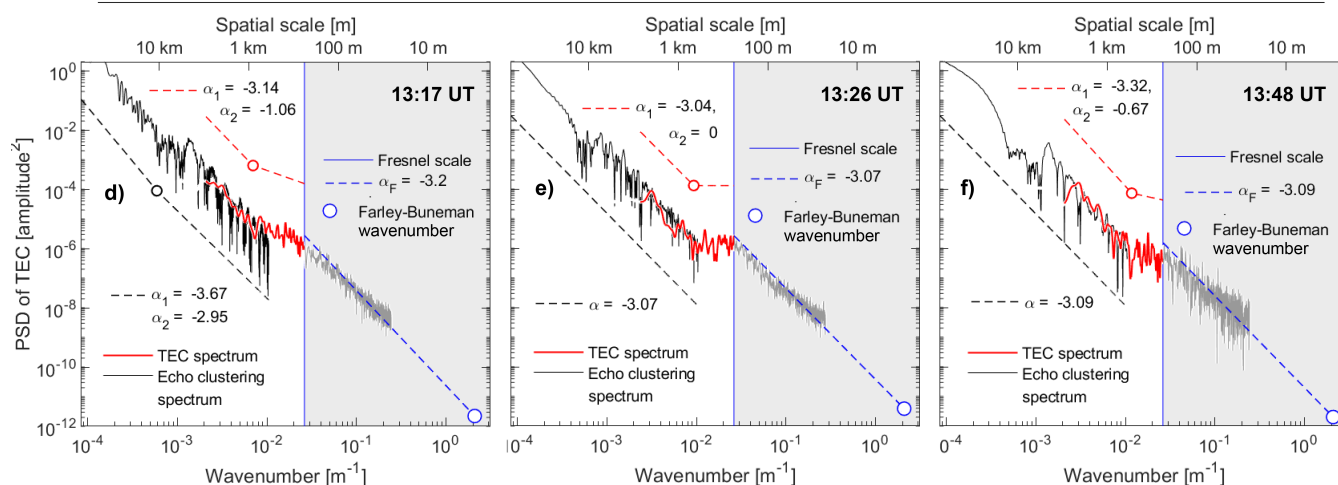


Figure A1. Six simultaneous ground-ground conjunctions between the ICEBEAR radar and observations from the CHAIN ISMR in Rabbit Lake. Each panel compares the spectral density measurements, the internal structure of the radar point-clouds denoted by a black line and the spectrum of GPS amplitude fluctuations in red and gray colors. The spectral indices are calculated automatically following Ivarsen et al. (2019) and are indicated, as is the Fresnel-scale.



Appendix B: Extended ICEBEAR-CHAIN-Swarm conjunction

We shall describe two successive space-ground-ground conjunctions that offer a clear, physical interpretation of the composite spectra. Figure B1 details two triple conjunctions between ICEBEAR, CHAIN, and the European Space Agency's Swarm mission (Friis-Christensen et al., 2006; Wood et al., 2022), consisting of three polar orbiting satellites (inclination 87° , altitude \sim 475 450 km, and orbital period of 90 minutes).

The conjunctions, with their geospatial coordinates detailed in Figure B1c), exhibited very strong magnetic fluctuations perpendicular to Earth's magnetic field, produced by field-aligned currents, and what follows is a treatment of the structure, or *filamentation*, of those currents.

Following Ivarsen et al. (2023a) and Ivarsen et al. (2024a), we Fourier analyze the Swarm 50 Hz magnetic field fluctuations 480 transformed into a mean-field-aligned coordinate system (Park et al., 2017; Ivarsen et al., 2020), and this Fourier analysis yields information on electrical current filamentation, the degree to which the observed currents are non-laminar, or anomalous. The quantity is analogous to the structuring of magnetic field-tubes in the plane perpendicular to the geomagnetic field. Figure B1a, f) detail the observed magnitude of the perpendicular magnetic fluctuations, with the distribution of simultaneously observed ICEBEAR echoes superposed with a red line.

485 As the Swarm satellites orbit through the topside (F-region) ionosphere with a velocity of $v_s = 7.62$ km/s, we apply Taylor's "frozen-in"-hypothesis to convert the temporal powerspectra to k -spectra. These are superposed on the ICEBEAR echo clustering spectra in Figure B1b, g), showing reasonable agreement on a wide range of spatial scales, that is, between 10^5 m and 750 m. We again note a good shape-wise agreement between the radar clustering spectra and the observed field-aligned current structures (filaments), echoing recent studies (Ivarsen et al., 2023a, 2024a). The implications are that the spatial characteristics 490 of turbulence in the E-region are contained, communicated, or embedded, by filaments in the field-aligned currents.

In Figure B1d, e), we compare the ICEBEAR and GPS spectra, for which the simultaneous conjunction took place between the two satellites' orbit, and which again exhibit excellent shape-wise agreement down to individual spectral features around 1 kilometer (inset panel e).

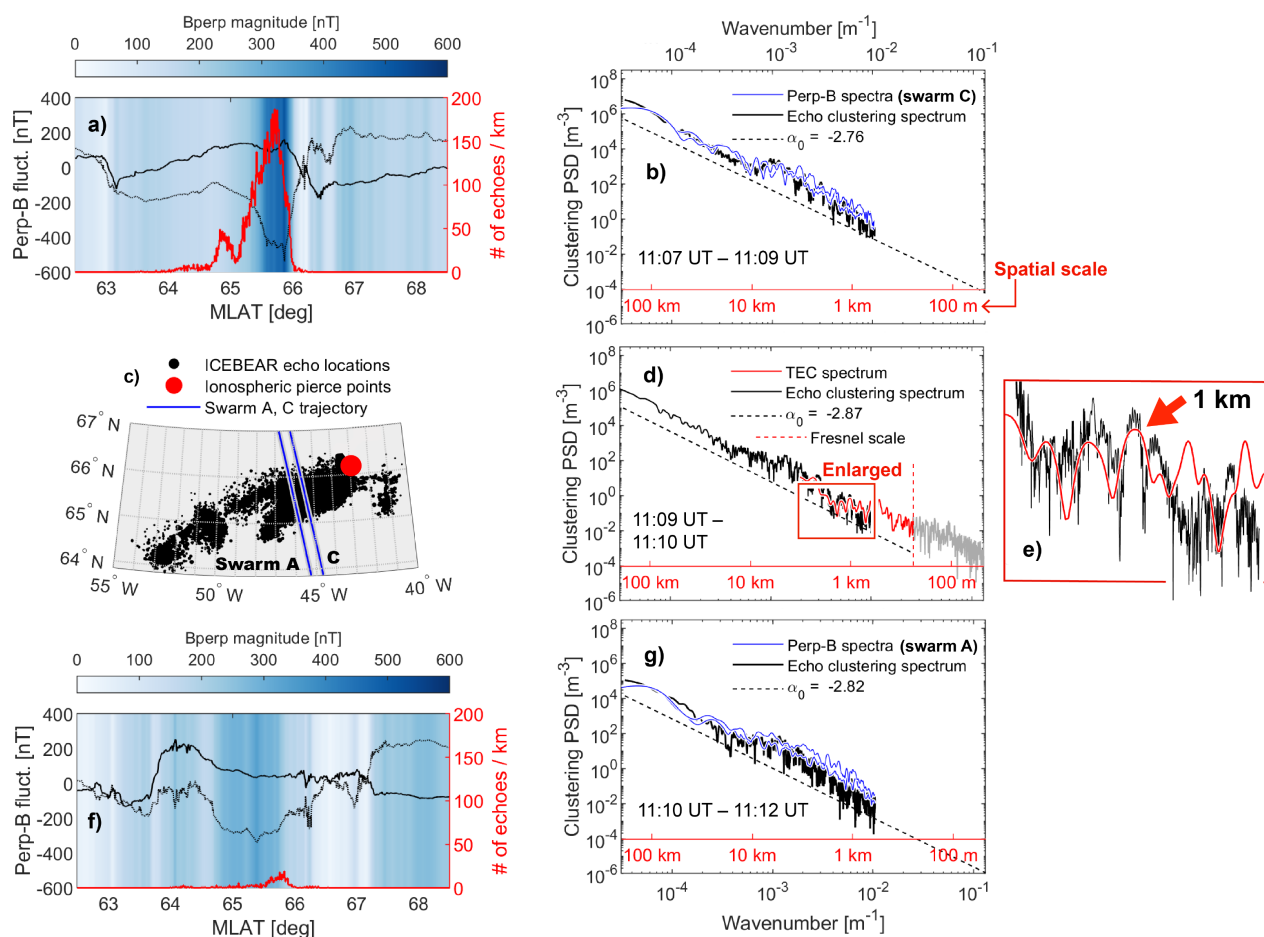


Figure B1. Two space-ground-ground conjunctions, and one ground-ground-conjunction, between ICEBEAR, a CHAIN ISMR, and the Swarm A and C satellites, on 6 May 2023. Panel b) shows the spatial distribution of echoes (black point-cloud), with the Swarm satellite orbits (blue lines) and GPS pierce-point (red circle) superposed. Panels a) and f) show the magnitude of the perpendicular magnetic fluctuations observed by the Swarm satellites (black line and blue colorscale), with the latitudinal distribution of ICEBEAR echoes superposed in red. Panels b, d, e, and g) show various composite powerspectra, with ICEBEAR clustering spectra (black), compared to CHAIN k -spectra (red, gray) and field-aligned current structuring spectra (blue) measured by Swarm. Panel e) shows an enlarged portion of the composite ICEBEAR-CHAIN spectrum in panel d).



Appendix C: Sensitivity of the Fresnel scale and scan velocity to the assumed irregularity altitude

495 In Section 2.3, we derived the corrected Fresnel scale λ_F (Eq. 3) and the phase-screen scan velocity $v_d = f_F \lambda_F$, where f_F is the Fresnel frequency derived from the data, and we did so under the assumption of a single, thin irregularity layer at altitude $h = 105$ km. Because the ICEBEAR echo altitude distribution (Figure 9c) spans roughly 95–110 km with an overall peak near 105 km (Ivarsen et al., 2023c), it is important to quantify how sensitive these derived quantities are to the thin layer assumption.

From Eq. (3), $\lambda_F \propto \sqrt{h}$, with the satellite elevation angle θ entering as a multiplicative factor in the denominator. The
500 fractional error in λ_F due to an altitude offset Δh from the assumed value $h_0 = 105$ km is therefore

$$\frac{\delta \lambda_F}{\lambda_F} = \sqrt{1 + \frac{\Delta h}{h_0}} - 1, \quad (C1)$$

which is independent of θ , and v_d subsequently inherits the same fractional sensitivity. Figure C1 confirms this: panel a) shows λ_F evaluated across the 90–120 km altitude range for representative elevation angles, while panel b) shows that the relative error curves for all θ collapse onto a single curve. A physically significant ± 5 km deviation from the assumed altitude
505 introduces a relative error of less than 2.5%, corresponding to a scan-velocity uncertainty of approximately ± 10 m/s for a typical observed drift of 500 m/s. This uncertainty is small compared to typical values of the E-region ion-acoustic speed (~ 400 – 500 m/s). In wavenumber space, a 2.5% shift in λ_F displaces the Fresnel break-point by ~ 0.01 decades in k .

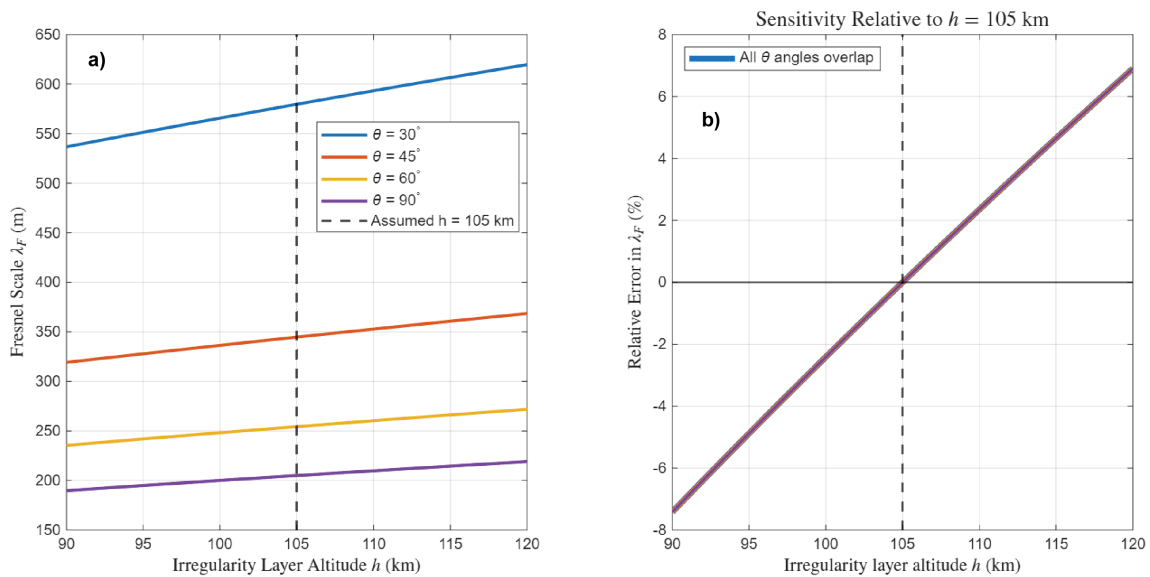


Figure C1. Panel a): λ_F as a function of altitude, for representative elevation angles. **Panel b):** the relative error curves (Eq. C1) for all θ .



Author contributions. MFI conceived of the study, performed data analysis, and wrote the manuscript. KS analyzed conjunctions, collected data, and developed analysis tools. LS developed analysis tools and provided feedback on the manuscript. DRT performed analysis and provided feedback on the manuscript. PTJ operated GNSS instrumentation and provided feedback on the manuscript. JP-ST, YS, YM, & DRH contributed comments and feedback on the manuscript. MFI, JP-ST, DRH, BP, SM, & GCH operated the ICEBEAR radar and provided data handling; GCH conceived of the radar. SK, KK, YM, TH, AS, KY, AM, YKaz, S-YW, IS, TM, TT, SY, & YKas designed and operated the Arase satellite and provided data handling.

Competing interests. At least one of the (co-)authors is a member of the editorial board of *Annales Geophysicae*.

Data availability Science data of the ERG (Arase) satellite were obtained from the ERG Science Center operated by ISAS/JAXA and ISEE/Nagoya University (Miyoshi et al., 2018a)(<https://ergsc.isee.nagoya-u.ac.jp/index.shtml.en>). This includes Lv.3 HEP (DOI 10.34515/DATA.ERG-01002) version 01_01, Lv.3 MEP-e (DOI 10.34515/DATA.ERG-02003) version 01_01, Lv.2 LEP-e (DOI 10.34515/DATA.ERG-05000) version 04_01, Lv.2 PWE/OFA (DOI 10.34515/DATA.ERG-08000), and Lv.2 MGF (DOI 10.34515/DATA.ERG-06001) version 04_04. SuperMAG data can be accessed at <https://supermag.jhuapl.edu/mag/>. ICEBEAR 3D echo data for 2020, 2021 is published with DOI 10.5281/zenodo.7509022. CHAIN ISMR data is available at <https://chain-new.chain-project.net/index.php/data-products/data-download>.

Acknowledgements. This work is supported in part by the European Space Agency's Living Planet Grant No. 1000012348 and by the Research Council of Norway (RCN) Grant No. 324859. We acknowledge the support of the Canadian Space Agency (CSA) [20SUGOICEB], the Canada Foundation for Innovation (CFI) John R. Evans Leaders Fund [32117], the Natural Science and Engineering Research Council (NSERC), the Discovery grants program [RGPIN-2019-19135], the Digital Research Alliance of Canada [RRG-4802]. DRT is supported through UK Natural Environment Research Council DRIIVE [NE/W003368/1] and FINESSE [NE/W003147/1] grants. MFI is grateful to J. Park and R. Horne for stimulating discussions.



References

- Baddour, N.: Chapter 1 - Two-Dimensional Fourier Transforms in Polar Coordinates, in: Advances in Imaging and Electron Physics, edited
530 by Hawkes, P. W., vol. 165 of *Imaging and Electron Physics*, pp. 1–45, Elsevier, <https://doi.org/10.1016/B978-0-12-385861-0.00001-4>,
2011.
- Baker, K. B. and Wing, S.: A New Magnetic Coordinate System for Conjugate Studies at High Latitudes, *Journal of Geophysical Research: Space Physics*, 94, 9139–9143, <https://doi.org/10.1029/JA094iA07p09139>, 1989.
- Barron, J. L., Fleet, D. J., and Beauchemin, S. S.: Performance of Optical Flow Techniques, *International Journal of Computer Vision*, 12,
535 43–77, <https://doi.org/10.1007/BF01420984>, 1994.
- Basu, S., Basu, S., MacKenzie, E., Coley, W. R., Sharber, J. R., and Hoegy, W. R.: Plasma Structuring by the Gradient Drift Instability at High Latitudes and Comparison with Velocity Shear Driven Processes, *Journal of Geophysical Research: Space Physics*, 95, 7799–7818, <https://doi.org/10.1029/JA095iA06p07799>, 1990.
- Blinstrubas, G., English, A., Stuart, D. J., Hampton, D. L., Lamarche, L., Nishimura, Y., and Datta-Barua, S.: Comparative Hypothesis
540 Testing of Auroral Ionospheric Layer Causing Global Navigation Satellite System Scintillation, *Space Weather*, 23, e2024SW004069, <https://doi.org/10.1029/2024SW004069>, 2025.
- Boldyrev, S. and Perez, J. C.: SPECTRUM OF KINETIC-ALFVÉN TURBULENCE, *The Astrophysical Journal Letters*, 758, L44, <https://doi.org/10.1088/2041-8205/758/2/L44>, 2012.
- Bougard, B., Sleewaegen, J.-M., Spogli, L., Veetil, S. V., and Monico, J. F. G.: CIGALA: Challenging the Solar Maximum in Brazil with
545 PolaRxS, in: Proceedings of the 24th International Technical Meeting of the Satellite Division of The Institute of Navigation (ION GNSS 2011), pp. 2572–2579, 2011.
- Buneman, O.: Excitation of Field Aligned Sound Waves by Electron Streams, *Physical Review Letters*, 10, 285–287, <https://doi.org/10.1103/PhysRevLett.10.285>, 1963.
- Chau, J. L. and St.-Maurice, J.-P.: Unusual 5 m E Region Field-Aligned Irregularities Observed from Northern Germany during the Magnetic
550 Storm of 17 March 2015, *Journal of Geophysical Research: Space Physics*, 121, 10,316–10,340, <https://doi.org/10.1002/2016JA023104>,
2016.
- Chen, L., Wu, D. J., and Huang, J.: Kinetic Alfvén Wave Instability Driven by Field-Aligned Currents in a Low- β Plasma, *Journal of Geophysical Research: Space Physics*, 118, 2951–2957, <https://doi.org/10.1002/jgra.50332>, 2013.
- Dahlgren, H., Lanchester, B. S., Ivchenko, N., and Whiter, D. K.: Variations in Energy, Flux, and Brightness of Pulsating Aurora Measured
555 at High Time Resolution, *Annales Geophysicae*, 35, 493–503, <https://doi.org/10.5194/angeo-35-493-2017>, 2017.
- David, V. and Galtier, S.: $K_{\perp}^{-8/3}$ Spectrum in Kinetic Alfvén Wave Turbulence: Implications for the Solar Wind, *The Astrophysical Journal Letters*, 880, L10, <https://doi.org/10.3847/2041-8213/ab2fe6>, 2019.
- D’Errico, J.: SLM-shape Language Modeling, SLM-Shape Language Modeling.. <http://www.mathworks.com/matlabcentral/fileexchange/24443-slm-shape-language-modeling>: Mathworks, 2009.
- 560 Dimant, Y. S. and Sudan, R. N.: Kinetic Theory of the Farley-Buneman Instability in the E Region of the Ionosphere, *Journal of Geophysical Research: Space Physics*, 100, 14 605–14 623, <https://doi.org/10.1029/95JA00794>, 1995.
- Drexler, J., St.-Maurice, J.-P., Chen, D., and Moorcroft, D. R.: New Insights from a Nonlocal Generalization of the Farley-Buneman Instability Problem at High Latitudes, *Annales Geophysicae*, 20, 2003–2025, <https://doi.org/10.5194/angeo-20-2003-2002>, 2002.



- Fang, X., Randall, C. E., Lummerzheim, D., Wang, W., Lu, G., Solomon, S. C., and Frahm, R. A.: Parameterization of Monoenergetic
565 Electron Impact Ionization, *Geophysical Research Letters*, 37, <https://doi.org/10.1029/2010GL045406>, 2010.
- Farley, D. T.: A Plasma Instability Resulting in Field-Aligned Irregularities in the Ionosphere, *Journal of Geophysical Research (1896-1977)*,
68, 6083–6097, <https://doi.org/10.1029/JZ068i022p06083>, 1963.
- Fejer, B. G. and Kelley, M. C.: Ionospheric Irregularities, *Reviews of Geophysics*, 18, 401–454, <https://doi.org/10.1029/RG018i002p00401>,
1980.
- 570 Forte, B. and Radicella, S. M.: Problems in Data Treatment for Ionospheric Scintillation Measurements, *Radio Science*, 37, 8–1–8–5,
<https://doi.org/10.1029/2001RS002508>, 2002.
- Foster, J. C. and Erickson, P. J.: Simultaneous Observations of E-region Coherent Backscatter and Electric Field Amplitude at F-region
Heights with the Millstone Hill UHF Radar, *Geophysical Research Letters*, 27, 3177–3180, <https://doi.org/10.1029/2000GL000042>, 2000.
- Fredricks, R. W. and Coroniti, F. V.: Ambiguities in the Deduction of Rest Frame Fluctuation Spectrums from Spectrums Computed in
575 Moving Frames, *Journal of Geophysical Research (1896-1977)*, 81, 5591–5595, <https://doi.org/10.1029/JA081i031p05591>, 1976.
- Friis-Christensen, E., Lühr, H., and Hulot, G.: Swarm: A Constellation to Study the Earth’s Magnetic Field, *Earth, Planets and Space*, 58,
BF03351 933, <https://doi.org/10.1186/BF03351933>, 2006.
- Galtier, S. and Meyrand, R.: Entanglement of Helicity and Energy in Kinetic Alfvén Wave/Whistler Turbulence, *Journal of Plasma Physics*,
81, 325810 106, <https://doi.org/10.1017/S0022377814000774>, 2015.
- 580 Ghidoni, R., Spogli, L., Mevius, M., Cesaroni, C., Alfonsi, L., Beser, K., Guerra, M., and Maestri, T.: Ionospheric Response
to the January 2022 Geomagnetic Storm Using LOFAR and GNSS, *Journal of Space Weather and Space Climate*, 15, 50,
<https://doi.org/10.1051/swsc/2025052>, 2025.
- Ghobadi, H., Spogli, L., Alfonsi, L., Cesaroni, C., Cicone, A., Linty, N., Romano, V., and Cafaro, M.: Disentangling Iono-
spheric Refraction and Diffraction Effects in GNSS Raw Phase through Fast Iterative Filtering Technique, *GPS Solutions*, 24, 85,
585 <https://doi.org/10.1007/s10291-020-01001-1>, 2020.
- Gillies, D. M., Knudsen, D., Spanswick, E., Donovan, E., Burchill, J., and Patrick, M.: Swarm Observations of Field-
Aligned Currents Associated with Pulsating Auroral Patches, *Journal of Geophysical Research: Space Physics*, 120, 9484–9499,
<https://doi.org/10.1002/2015JA021416>, 2015.
- Gillies, D. M., Liang, J., Donovan, E., and Spanswick, E.: The Apparent Motion of STEVE and the Picket Fence Phenomena, *Geophysical*
590 *Research Letters*, 47, e2020GL088 980, <https://doi.org/10.1029/2020GL088980>, 2020.
- Hamza, A. M. and St-Maurice, J. P.: A Turbulent Theoretical Framework for the Study of Current-Driven E Region Irregularities at High
Latitudes: Basic Derivation and Application to Gradient-Free Situations, *Journal of Geophysical Research: Space Physics*, 98, 11 587–
11 599, <https://doi.org/10.1029/92JA02836>, 1993.
- Hamza, A. M., Song, K., Meziane, K., and Thayyil, J. P.: Two-Component Phase Scintillation Spectra in the Auroral Region: Observations
595 and Model, Preprint, Preprints, <https://doi.org/10.22541/essoar.169272227.79637429/v1>, 2023.
- Hosokawa, K. and Ogawa, Y.: Ionospheric Variation during Pulsating Aurora, *Journal of Geophysical Research: Space Physics*, 120, 5943–
5957, <https://doi.org/10.1002/2015JA021401>, 2015.
- Huba, J. D., Hassam, A. B., Schwartz, I. B., and Keskinen, M. J.: Ionospheric Turbulence: Interchange Instabilities and Chaotic Fluid
Behavior, *Geophysical Research Letters*, 12, 65–68, <https://doi.org/10.1029/GL012i001p00065>, 1985.
- 600 Hultqvist, B. and Egeland, A.: Radio Aurora, *Space Science Reviews*, 3, 27–78, <https://doi.org/10.1007/BF00226644>, 1964.



- Huyghebaert, D., Hussey, G., Vierinen, J., McWilliams, K., and St-Maurice, J.-P.: ICEBEAR: An All-Digital Bistatic Coded Continuous-Wave Radar for Studies of the E Region of the Ionosphere, *Radio Science*, 54, 349–364, <https://doi.org/10.1029/2018RS006747>, 2019.
- Ivarsen, M. F.: A Source or a Sink? How the Altitude of Particle Precipitation Influence High-Latitude Electrodynamics, *Annales Geophysicae*, 44, 149–162, <https://doi.org/10.5194/angeo-44-149-2026>, 2026.
- 605 Ivarsen, M. F., Bull, P., Llinares, C., and Mota, D. F.: Distinguishing Screening Mechanisms with Environment-Dependent Velocity Statistics, *Astronomy & Astrophysics*, 595, A40, <https://doi.org/10.1051/0004-6361/201628604>, 2016.
- Ivarsen, M. F., Jin, Y., Spicher, A., and Clausen, L. B. N.: Direct Evidence for the Dissipation of Small-Scale Ionospheric Plasma Structures by a Conductive E Region, *Journal of Geophysical Research: Space Physics*, 124, 2935–2942, <https://doi.org/10.1029/2019JA026500>, 2019.
- 610 Ivarsen, M. F., Park, J., Kwak, Y.-S., Jin, Y., Knudsen, D. J., and Clausen, L. B. N.: Observational Evidence for the Role of Hall Conductance in Alfvén Wave Reflection, *Journal of Geophysical Research: Space Physics*, 125, e2020JA028119, <https://doi.org/10.1029/2020JA028119>, 2020.
- Ivarsen, M. F., St-Maurice, J.-P., Jin, Y., Park, J., Miloch, W., Spicher, A., Kwak, Y.-S., and Clausen, L. B. N.: Steepening Plasma Density Spectra in the Ionosphere: The Crucial Role Played by a Strong E-Region, *Journal of Geophysical Research: Space Physics*, 126, e2021JA029401, <https://doi.org/10.1029/2021JA029401>, 2021.
- 615 Ivarsen, M. F., Lozinsky, A., St-Maurice, J.-P., Spicher, A., Huyghebaert, D., Hussey, G. C., Galeschuk, D., Pitzel, B., and Vierinen, J.: The Distribution of Small-Scale Irregularities in the E-Region, and Its Tendency to Match the Spectrum of Field-Aligned Current Structures in the F-Region, *Journal of Geophysical Research: Space Physics*, 128, e2022JA031233, <https://doi.org/10.1029/2022JA031233>, 2023a.
- Ivarsen, M. F., St-Maurice, J.-P., Hussey, G., Spicher, A., Jin, Y., Lozinsky, A., Goodwin, L. V., Galeschuk, D., Park, J., and Clausen, L. B. N.: Measuring Small-Scale Plasma Irregularities in the High-Latitude E- and F-regions Simultaneously, *Scientific Reports*, 13, 11 579, <https://doi.org/10.1038/s41598-023-38777-4>, 2023b.
- 620 Ivarsen, M. F., St-Maurice, J.-P., Hussey, G. C., Galeschuk, D., Lozinsky, A., Pitzel, B., and McWilliams, K. A.: An Algorithm to Separate Ionospheric Turbulence Radar Echoes From Those of Meteor Trails in Large Data Sets, *Journal of Geophysical Research: Space Physics*, 128, e2022JA031050, <https://doi.org/10.1029/2022JA031050>, 2023c.
- 625 Ivarsen, M. F., Gillies, M. D., Huyghebaert, D. R., St-Maurice, J.-P., Lozinsky, A., Galeschuk, D., Donovan, E., and Hussey, G. C.: Turbulence Embedded Into the Ionosphere by Electromagnetic Waves, *Journal of Geophysical Research: Space Physics*, 129, e2023JA032310, <https://doi.org/10.1029/2023JA032310>, 2024a.
- Ivarsen, M. F., Huyghebaert, D. R., Gillies, M. D., St-Maurice, J.-P., Themens, D. R., Oppenheim, M., Gustavsson, B. J., Billett, D., Pitzel, B., Galeschuk, D., Donovan, E., and Hussey, G. C.: Turbulence Around Auroral Arcs, *Journal of Geophysical Research: Space Physics*, 129, e2023JA032309, <https://doi.org/10.1029/2023JA032309>, 2024b.
- 630 Ivarsen, M. F., St-Maurice, J.-P., Hussey, G. C., Huyghebaert, D. R., and Gillies, M. D.: Point-Cloud Clustering and Tracking Algorithm for Radar Interferometry, *Physical Review E*, 110, 045 207, <https://doi.org/10.1103/PhysRevE.110.045207>, 2024c.
- Ivarsen, M. F., St-Maurice, J.-P., Huyghebaert, D. R., Gillies, M. D., Lind, F., Pitzel, B., and Hussey, G. C.: Deriving the Ionospheric Electric Field From the Bulk Motion of Radar Aurora in the E-Region, *Journal of Geophysical Research: Space Physics*, 129, e2024JA033060, <https://doi.org/10.1029/2024JA033060>, 2024d.
- 635 Ivarsen, M. F., St-Maurice, J.-P., Jin, Y., Park, J., Buschman, L. M., and Clausen, L. B.: To What Degree Does the High-Energy Aurora Destroy F-region Irregularities?, *Frontiers in Astronomy and Space Sciences*, 11, <https://doi.org/10.3389/fspas.2024.1309136>, 2024e.



- Ivarsen, M. F., Miyashita, Y., St-Maurice, J.-P., Hussey, G. C., Pitzel, B., Galeschuk, D., Marei, S., Horne, R. B., Kasahara, Y., Matsuda, S., Kasahara, S., Keika, K., Miyoshi, Y., Yamamoto, K., Shinbori, A., Huyghebaert, D. R., Matsuoka, A., Yokota, S., and Tsuchiya, F.: Characteristic E-Region Plasma Signature of Magnetospheric Wave-Particle Interactions, *Physical Review Letters*, 134, 145 201, <https://doi.org/10.1103/PhysRevLett.134.145201>, 2025a.
- Ivarsen, M. F., St-Maurice, J.-P., Hussey, G. C., Billet, D., Huyghebaert, D. R., Jin, Y., Miyashita, Y., Kasahara, S., Song, K., Jayachandran, P. T., Yokota, S., Miyoshi, Y., Yamamoto, K., Shinbori, A., Kasahara, Y., Shinohara, I., and Matsuoka, A.: Eastward Transients in the Dayside Ionosphere. I. Electrodynamics on Closed Field Lines, *Physical Review E*, 112, 045 204, <https://doi.org/10.1103/r6bv-pzfq>, 2025b.
- Ivarsen, M. F., St-Maurice, J.-P., Hussey, G. C., McWilliams, K., Jin, Y., Huyghebaert, D. R., Miyashita, Y., and Sibeck, D.: Eastward Transients in the Dayside Ionosphere. II. A Parallel-Plate Capacitorlike Effect, *Physical Review E*, 112, 045 203, <https://doi.org/10.1103/3bjz-bsf8>, 2025c.
- Jayachandran, P. T., Langley, R. B., MacDougall, J. W., Mushini, S. C., Pokhotelov, D., Hamza, A. M., Mann, I. R., Milling, D. K., Kale, Z. C., Chadwick, R., Kelly, T., Danskin, D. W., and Carrano, C. S.: Canadian High Arctic Ionospheric Network (CHAIN), *Radio Science*, 44, <https://doi.org/10.1029/2008RS004046>, 2009.
- Jin, Y., Moen, J. I., and Miloch, W. J.: GPS Scintillation Effects Associated with Polar Cap Patches and Substorm Auroral Activity: Direct Comparison, *Journal of Space Weather and Space Climate*, 4, A23, <https://doi.org/10.1051/swsc/2014019>, 2014.
- Kasahara, S., Yokota, S., Mitani, T., Asamura, K., Hirahara, M., Shibano, Y., and Takashima, T.: Medium-Energy Particle Experiments—Electron Analyzer (MEP-e) for the Exploration of Energization and Radiation in Geospace (ERG) Mission, *Earth, Planets and Space*, 70, 69, <https://doi.org/10.1186/s40623-018-0847-z>, 2018.
- Kawamura, Y., Hosokawa, K., Nozawa, S., Ogawa, Y., Kawabata, T., Oyama, S.-I., Miyoshi, Y., Kurita, S., and Fujii, R.: Estimation of the Emission Altitude of Pulsating Aurora Using the Five-Wavelength Photometer, *Earth, Planets and Space*, 72, 96, <https://doi.org/10.1186/s40623-020-01229-8>, 2020.
- Kazama, Y., Wang, B.-J., Wang, S.-Y., Ho, P. T. P., Tam, S. W. Y., Chang, T.-F., Chiang, C.-Y., and Asamura, K.: Low-Energy Particle Experiments—Electron Analyzer (LEPe) Onboard the Arase Spacecraft, *Earth, Planets and Space*, 69, 165, <https://doi.org/10.1186/s40623-017-0748-6>, 2017.
- Keskinen, M. J.: Nonlinear Stabilization of the Farley-Buneman Instability by Strong $E \times B$ Turbulence., Tech. rep., 1981.
- Keskinen, M. J. and Huba, J. D.: Nonlinear Evolution of High-Latitude Ionospheric Interchange Instabilities with Scale-Size-Dependent Magnetospheric Coupling, *Journal of Geophysical Research: Space Physics*, 95, 15 157–15 166, <https://doi.org/10.1029/JA095iA09p15157>, 1990.
- Kintner P. M., Ledvina B. M., and de Paula E. R.: GPS and Ionospheric Scintillations, *Space Weather*, 5, <https://doi.org/10.1029/2006SW000260>, 2007.
- Kivanc and Heelis, R. A.: Spatial Distribution of Ionospheric Plasma and Field Structures in the High-Latitude F Region, *Journal of Geophysical Research*, 103, 6955–6968, <https://doi.org/10.1029/97JA03237>, 1998.
- Krämer, E., Koller, F., Suni, J., LaMoury, A. T., Pöppelwerth, A., Glebe, G., Mohammed-Amin, T., Raptis, S., Vuorinen, L., Weiss, S., Xirogiannopoulou, N., Archer, M., Blanco-Cano, X., Gunell, H., Hietala, H., Karlsson, T., Plaschke, F., Preisser, L., Roberts, O., Simon Wedlund, C., Temmer, M., and Vörös, Z.: Jets Downstream of Collisionless Shocks: Recent Discoveries and Challenges, *Space Science Reviews*, 221, 4, <https://doi.org/10.1007/s11214-024-01129-3>, 2024.



- 675 Lozinsky, A., Hussey, G., McWilliams, K., Huyghebaert, D., and Galeschuk, D.: ICEBEAR-3D: A Low Elevation Imaging Radar Using a Non-Uniform Coplanar Receiver Array for E Region Observations, *Radio Science*, 57, e2021RS007358, <https://doi.org/10.1029/2021RS007358>, 2022.
- Marek, M. and Schreiber, R.: Can the Auroral Kilometric Radiation Be a Self-Organized Criticality System?, *Earth and Space Science*, 9, e2021EA002148, <https://doi.org/10.1029/2021EA002148>, 2022.
- 680 Marov, M. Y. and Kolesnichenko, A. V.: Self-Organization of Developed Turbulence and Formation Mechanisms of Coherent Structures, in: *Turbulence and Self-Organization: Modeling Astrophysical Objects*, edited by Marov, M. Y. and Kolesnichenko, A. V., pp. 373–423, Springer, New York, NY, ISBN 978-1-4614-5155-6, https://doi.org/10.1007/978-1-4614-5155-6_6, 2013.
- Maynard, N. C., Bahnsen, A., Christophersen, P., Egeland, A., and Lundin, R.: An Example of Anticorrelation of Auroral Particles and Electric Fields, *J. Geophys. Res.*, v. 78, no. 19, pp. 3976–3980, <https://doi.org/10.1029/JA078i019p03976>, 1973.
- 685 McCaffrey, A. M. and Jayachandran, P. T.: Determination of the Refractive Contribution to GPS Phase “Scintillation”, *Journal of Geophysical Research: Space Physics*, 124, 1454–1469, <https://doi.org/10.1029/2018JA025759>, 2019.
- Meziane, K., Hamza, A. M., and Jayachandran, P. T.: Turbulence Signatures in High-Latitude Ionospheric Scintillation, *Journal of Geophysical Research: Space Physics*, 128, e2022JA030934, <https://doi.org/10.1029/2022JA030934>, 2023.
- Mitani, T., Takashima, T., Kasahara, S., Miyake, W., and Hirahara, M.: High-Energy Electron Experiments (HEP) Aboard the ERG (Arase) Satellite, *Earth, Planets and Space*, 70, 77, <https://doi.org/10.1186/s40623-018-0853-1>, 2018.
- Miyoshi, Y., Hori, T., Shoji, M., Teramoto, M., Chang, T. F., Segawa, T., Umemura, N., Matsuda, S., Kurita, S., Keika, K., Miyashita, Y., Seki, K., Tanaka, Y., Nishitani, N., Kasahara, S., Yokota, S., Matsuoka, A., Kasahara, Y., Asamura, K., Takashima, T., and Shinohara, I.: The ERG Science Center, *Earth, Planets and Space*, 70, 96, <https://doi.org/10.1186/s40623-018-0867-8>, 2018a.
- Miyoshi, Y., Shinohara, I., Takashima, T., Asamura, K., Higashio, N., Mitani, T., Kasahara, S., Yokota, S., Kazama, Y., Wang, S.-Y., Tam, S. W. Y., Ho, P. T. P., Kasahara, Y., Kasaba, Y., Yagitani, S., Matsuoka, A., Kojima, H., Katoh, Y., Shiokawa, K., and Seki, K.: Geospace Exploration Project ERG, *Earth, Planets and Space*, 70, 101, <https://doi.org/10.1186/s40623-018-0862-0>, 2018b.
- Miyoshi, Y., Shinohara, I., Ukhorskiy, S., Claudepierre, S. G., Mitani, T., Takashima, T., Hori, T., Santolik, O., Kolmasova, I., Matsuda, S., Kasahara, Y., Teramoto, M., Katoh, Y., Hikishima, M., Kojima, H., Kurita, S., Imajo, S., Higashio, N., Kasahara, S., Yokota, S., Asamura, K., Kazama, Y., Wang, S.-Y., Jun, C.-W., Kasaba, Y., Kumamoto, A., Tsuchiya, F., Shoji, M., Nakamura, S., Kitahara, M., Matsuoka, A., Shiokawa, K., Seki, K., Nosé, M., Takahashi, K., Martinez-Calderon, C., Hospodarsky, G., Colpitts, C., Kletzing, C., Wygant, J., Spence, H., Baker, D. N., Reeves, G. D., Blake, J. B., and Lanzerotti, L.: Collaborative Research Activities of the Arase and Van Allen Probes, *Space Science Reviews*, 218, 38, <https://doi.org/10.1007/s11214-022-00885-4>, 2022.
- 700 Moen, J., Oksavik, K., Alfonsi, L., Daabakk, Y., Romano, V., and Spogli, L.: Space Weather Challenges of the Polar Cap Ionosphere, *Journal of Space Weather and Space Climate*, 3, A02, <https://doi.org/10.1051/swsc/2013025>, 2013.
- 705 Mounir, H., Berthelier, A., Cerisier, J. C., Lagoutte, D., and Beghin, C.: The Small-Scale Turbulent Structure of the High Latitude Ionosphere - Arcad-Aureol-3 Observations, *Annales Geophysicae*, 9, 725–737, 1991.
- Nishimura, Y., Lessard, M. R., Katoh, Y., Miyoshi, Y., Grono, E., Partamies, N., Sivasdas, N., Hosokawa, K., Fukizawa, M., Samara, M., Michell, R. G., Kataoka, R., Sakanoi, T., Whiter, D. K., Oyama, S.-i., Ogawa, Y., and Kurita, S.: Diffuse and Pulsating Aurora, *Space Science Reviews*, 216, 4, <https://doi.org/10.1007/s11214-019-0629-3>, 2020.
- 710 Oppenheim, M. M. and Dimant, Y. S.: Kinetic Simulations of 3-D Farley-Buneman Turbulence and Anomalous Electron Heating, *Journal of Geophysical Research: Space Physics*, 118, 1306–1318, <https://doi.org/10.1002/jgra.50196>, 2013.



- Pakhotin, I. P., Mann, I. R., Lysak, R. L., Knudsen, D. J., Gjerloev, J. W., Rae, I. J., Forsyth, C., Murphy, K. R., Miles, D. M., Ozeke, L. G., and Balasis, G.: Diagnosing the Role of Alfvén Waves in Magnetosphere-Ionosphere Coupling: Swarm Observations of Large Amplitude Nonstationary Magnetic Perturbations During an Interval of Northward IMF, *Journal of Geophysical Research: Space Physics*, 123, 326–340, <https://doi.org/10.1002/2017JA024713>, 2018.
- 715 Palmroth, M., Grandin, M., Sarris, T., Doornbos, E., Tourgaidis, S., Aikio, A., Buchert, S., Clilverd, M. A., Dandouras, I., Heelis, R., Hoffmann, A., Ivchenko, N., Kervalishvili, G., Knudsen, D. J., Kotova, A., Liu, H.-L., Malaspina, D. M., March, G., Marchaudon, A., Marghita, O., Matsuo, T., Miloch, W. J., Moretto-Jørgensen, T., Mpaloukidis, D., Olsen, N., Papadakis, K., Pfaff, R., Pirmaris, P., Siemes, C., Stolle, C., Suni, J., van den IJssel, J., Verronen, P. T., Visser, P., and Yamauchi, M.: Lower-Thermosphere–Ionosphere (LTI) Quantities: Current Status of Measuring Techniques and Models, *Annales Geophysicae*, 39, 189–237, <https://doi.org/10.5194/angeo-39-189-2021>, 2021.
- 720 Park, J., Lühr, H., Knudsen, D. J., Burchill, J. K., and Kwak, Y.-S.: Alfvén Waves in the Auroral Region, Their Poynting Flux, and Reflection Coefficient as Estimated from Swarm Observations, *Journal of Geophysical Research: Space Physics*, 122, 2345–2360, <https://doi.org/10.1002/2016JA023527>, 2017.
- 725 Partamies, N., Whiter, D., Kadokura, A., Kauristie, K., Tyssøy, H. N., Massetti, S., Stauning, P., and Raita, T.: Occurrence and Average Behavior of Pulsating Aurora, *Journal of Geophysical Research: Space Physics*, 122, 5606–5618, <https://doi.org/10.1002/2017JA024039>, 2017.
- Phelps, A. D. R. and Sagalyn, R. C.: Plasma Density Irregularities in the High-Latitude Top Side Ionosphere, *Journal of Geophysical Research*, 81, 515–523, <https://doi.org/10.1029/JA081i004p00515>, 1976.
- 730 Prikryl, P., André, D., Sofko, G. J., and Koehler, J. A.: Doppler Radar Observations of Harmonics of Electrostatic Ion Cyclotron Waves in the Auroral Ionosphere, *Journal of Geophysical Research: Space Physics*, 93, 7409–7424, <https://doi.org/10.1029/JA093iA07p07409>, 1988.
- Prikryl, P., Andre, D., Koehler, J. A., Sofko, G. J., and McKibben, M. J.: Evidence of Highly Localized Auroral Scatterers from 50-MHz CW Radar Interferometry, *Planetary and space science*, 38, 933–944, 1990.
- Redmon, R. J., Denig, W. F., Kilcommons, L. M., and Knipp, D. J.: New DMSP Database of Precipitating Auroral Electrons and Ions, *Journal of Geophysical Research: Space Physics*, 122, 9056–9067, <https://doi.org/10.1002/2016JA023339>, 2017.
- 735 RGB, T.: UCalgary Space Remote Sensing Group Data Landing Page — UCalgary SRS Data Documentation, 2023.
- Robinson, T. R.: Towards a Self-Consistent Non-Linear Theory of Radar Auroral Backscatter, *Journal of Atmospheric and Terrestrial Physics*, 48, 417–422, [https://doi.org/10.1016/0021-9169\(86\)90118-2](https://doi.org/10.1016/0021-9169(86)90118-2), 1986.
- Sahr, J. D. and Fejer, B. G.: Auroral Electrojet Plasma Irregularity Theory and Experiment: A Critical Review of Present Understanding and Future Directions, *Journal of Geophysical Research: Space Physics*, 101, 26 893–26 909, <https://doi.org/10.1029/96JA02404>, 1996.
- 740 Sato, T.: Stabilization of the Two-Stream Instability in the Equatorial Electrojet, *Physical Review Letters*, 28, 732–734, <https://doi.org/10.1103/PhysRevLett.28.732>, 1972.
- Schlegel, K.: Auroral Zone E-region Conductivities during Solar Minimum Derived from EISCAT Data, *Ann. Geophys. (C.N.R.S.)*; (France), 6:1, 1988.
- 745 Shen, Y., Verkhoglyadova, O. P., Artemyev, A., Hartinger, M. D., Angelopoulos, V., Shi, X., and Zou, Y.: Magnetospheric Control of Ionospheric TEC Perturbations via Whistler-Mode and ULF Waves, *AGU Advances*, 5, e2024AV001 302, <https://doi.org/10.1029/2024AV001302>, 2024.
- Siscoe, G., Raeder, J., and Ridley, A. J.: Transpolar Potential Saturation Models Compared, *Journal of Geophysical Research: Space Physics*, 109, <https://doi.org/10.1029/2003JA010318>, 2004.



- 750 Song, K., Hamza, A. M., Jayachandran, P. T., Meziane, K., and Kashcheyev, A.: Spectral Characteristics of Phase Fluctuations at High Latitude, *Journal of Geophysical Research: Space Physics*, 128, e2022JA031244, <https://doi.org/10.1029/2022JA031244>, 2023.
- Song, K., Meziane, K., Hamza, A. M., and Jayachandran, P. T.: Investigation of the Fresnel Scale From Ionospheric Scintillation Spectra, *Journal of Geophysical Research: Space Physics*, 130, e2024JA033239, <https://doi.org/10.1029/2024JA033239>, 2025.
- Spicher, A., Miloch, W. J., and Moen, J. I.: Direct Evidence of Double-Slope Power Spectra in the High-Latitude Ionospheric Plasma, *Geophysical Research Letters*, 41, 1406–1412, <https://doi.org/10.1002/2014GL059214>, 2014.
- 755 Spogli, L., Ghobadi, H., Cicone, A., Alfonsi, L., Cesaroni, C., Linty, N., Romano, V., and Cafaro, M.: Adaptive Phase Detrending for GNSS Scintillation Detection: A Case Study over Antarctica, *IEEE Geoscience and Remote Sensing Letters*, 19, 1–5, 2021.
- St.-Maurice, J.-P. and Chau, J. L.: A Theoretical Framework for the Changing Spectral Properties of Meter-Scale Farley-Buneman Waves between 90 and 125 Km Altitudes, *Journal of Geophysical Research: Space Physics*, 121, 10,341–10,366, <https://doi.org/10.1002/2016JA023105>, 2016.
- 760 St.-Maurice, J.-P. and Goodwin, L.: Revisiting the Behavior of the E-Region Electron Temperature During Strong Electric Field Events at High Latitudes, *Journal of Geophysical Research: Space Physics*, 126, 2020JA028288, <https://doi.org/10.1029/2020JA028288>, 2021.
- St.-Maurice, J.-P. and Hamza, A. M.: A New Nonlinear Approach to the Theory of E Region Irregularities, *Journal of Geophysical Research: Space Physics*, 106, 1751–1759, <https://doi.org/10.1029/2000JA000246>, 2001.
- 765 St.-Maurice, J. P., Kofman, W., and Kluzek, E.: Electron Heating by Plasma Waves in the High Latitude E-region and Related Effects: Observations, *Advances in Space Research*, 10, 225–237, [https://doi.org/10.1016/0273-1177\(90\)90256-Y](https://doi.org/10.1016/0273-1177(90)90256-Y), 1990.
- St.-Maurice, J.-P., Huyghebaert, D., Ivarsen, M. F., and Hussey, G. C.: Narrow Width Farley-Buneman Spectra Above 100 Km Altitude, *Journal of Geophysical Research: Space Physics*, 128, e2022JA031191, <https://doi.org/10.1029/2022JA031191>, 2023.
- Sudan, R. N. and Keskinen, M.: Theory of Strongly Turbulent Two-Dimensional Convection of Low-Pressure Plasma, *Physical Review Letters*, 38, 966–970, <https://doi.org/10.1103/PhysRevLett.38.966>, 1977.
- 770 Sudan, R. N., Akinrimisi, J., and Farley, D. T.: Generation of Small-Scale Irregularities in the Equatorial Electrojet, *Journal of Geophysical Research (1896-1977)*, 78, 240–248, <https://doi.org/10.1029/JA078i001p00240>, 1973.
- Tesema, F., Partamies, N., Nesse Tyssøy, H., and McKay, D.: Observations of Precipitation Energies during Different Types of Pulsating Aurora, *Annales Geophysicae*, 38, 1191–1202, <https://doi.org/10.5194/angeo-38-1191-2020>, 2020.
- 775 Teunissen, P. J. and Montenbruck, O., eds.: *Springer Handbook of Global Navigation Satellite Systems*, Springer International Publishing, Cham, ISBN 978-3-319-42926-7 978-3-319-42928-1, <https://doi.org/10.1007/978-3-319-42928-1>, 2017.
- Themens, D. R., Jayachandran, P. T., Galkin, I., and Hall, C.: The Empirical Canadian High Arctic Ionospheric Model (E-CHAIM): NmF2 and hmF2, *Journal of Geophysical Research: Space Physics*, 122, 9015–9031, <https://doi.org/10.1002/2017JA024398>, 2017.
- Tsunoda, R. T.: High-Latitude F Region Irregularities: A Review and Synthesis, *Reviews of Geophysics*, 26, 719–760, <https://doi.org/10.1029/RG026i004p00719>, 1988.
- 780 Tsunoda, R. T., Livingston, R. C., McClure, J. P., and Hanson, W. B.: Equatorial Plasma Bubbles: Vertically Elongated Wedges from the Bottomside F Layer, *Journal of Geophysical Research: Space Physics*, 87, 9171–9180, <https://doi.org/10.1029/JA087iA11p09171>, 1982.
- Tsyganenko, N. A. and Sitnov, M. I.: Modeling the Dynamics of the Inner Magnetosphere during Strong Geomagnetic Storms, *Journal of Geophysical Research: Space Physics*, 110, 2004JA010798, <https://doi.org/10.1029/2004JA010798>, 2005.
- 785 Vickrey, J. F. and Kelley, M. C.: The Effects of a Conducting E Layer on Classical F Region Cross-Field Plasma Diffusion, *Journal of Geophysical Research: Space Physics*, 87, 4461–4468, <https://doi.org/10.1029/JA087iA06p04461>, 1982.



- Villain, J. P., Hanuise, C., and Beghin, C.: ARCAD3-SAFARI Coordinated Study of Auroral and Polar F-region Ionospheric Irregularities, *Annales Geophysicae*, 4, 61–68, 1986.
- 790 Wood, A. G., Alfonsi, L., Clausen, L. B. N., Jin, Y., Spogli, L., Urbář, J., Rawlings, J. T., Whittaker, I. C., Dorrian, G. D., Høeg, P., Kotova, D.,
Cesaroni, C., Cicone, A., Miedzik, J., Gierlach, E., Kochańska, P., Wojtkiewicz, P., Shahtahmassebi, G., and Miloch, W. J.: Variability of
Ionospheric Plasma: Results from the ESA Swarm Mission, *Space Science Reviews*, 218, 52, <https://doi.org/10.1007/s11214-022-00916-0>, 2022.
- Yeh, K. C. and Liu, C.-H.: Radio Wave Scintillations in the Ionosphere, *IEEE Proceedings*, 70, 324–360, 1982.
- 795 Zhang, Y. and Varney, R. H.: A Statistical Survey of E-Region Anomalous Electron Heating Using Poker Flat Incoherent Scatter Radar
Observations, *Journal of Geophysical Research: Space Physics*, 129, e2023JA032360, <https://doi.org/10.1029/2023JA032360>, 2024.